Stratified AGB Inversion Driven by DGTHI: Quantifying Topographic Controls on Biomass Prediction Across Tree Species

Yihan Zhu
Wuhan University
Jiangping Chen
chen_jp@whu.edu.cn
Wuhan University
Jianhua Yin
Wuhan University
Zilong Qin
Wuhan University
Jizhou Chen
Wuhan University
Na Jiang
Shandong Provincial Institute of Land Surveying and Mapping
Ke Hou
Shandong Provincial Institute of Land Surveying and Mapping

Research Article

Keywords: Aboveground Biomass, Topographic Heterogeneity, DGTHI, Species-Specific Modeling, LiDAR

Posted Date: August 20th, 2025

DOI: https://doi.org/10.21203/rs.3.rs-7185026/v1

Additional Declarations: No competing interests reported.

Stratified AGB Inversion Driven by DGTHI: Quantifying Topographic Controls on Biomass Prediction Across Tree Species

Author(s): Yihan Zhu[1], Jiangping Chen[1,*], Jianhua Yin[1], Zilong Qin[1], Jizhou Chen[1], Na Jiang[2] ,Ke Hou[2]

[1] School of Remote Sensing and Information Engineering, Wuhan University, Wuhan 430079, China

[2] Shandong Provincial Institute of Land Surveying and Mapping, Jinan, Shandong 250102, China

[*] Correspondence: chen_jp@whu.edu.cn;

Abstract

Accurate forest aboveground biomass (AGB) estimation is crucial for global carbon cycle research. While existing studies have utilized topographic factors in remote sensing, they often fail to systematically quantify multi-dimensional heterogeneity or address species-specific responses. This study pioneers the application of the Digital Elevation Model (DEM) Grid Topographic Heterogeneity Index (DGTHI) — a composite metric integrating elevation variability, relief, surface roughness, and mean slope — to enhance AGB inversion models by explicitly accounting for terrain-vegetation interactions. Using airborne Light detection and ranging (LiDAR) and 8,804 field-measured trees in Mengyin County, Linyi City, Shandong Province, China, we developed a DGTHI-stratified modeling framework to dissect how topographic heterogeneity governs species-level AGB estimation accuracy at the county scale.Results demonstrate: (1) DGTHI outperformed conventional single-factor topographic corrections, with heterogeneity effects on feature selection following a

species hierarchy: acacia > pine > cypress > poplar; (2) DGTHI-driven stratification significantly improved model accuracy, increasing R^2 by 0.08 – 0.17 versus unstratified models; (3) Spatial AGB patterns (27 – 217 t/ha in May 2023) revealed southwest – northeast highs and northwest – southeast lows, directly modulated by DGTHI-mapped heterogeneity. As the first integration of DGTHI into species-specific AGB inversion, this work provides a transferable paradigm for precision carbon mapping in topographically complex forests.

Keywords: Aboveground Biomass, Topographic Heterogeneity, DGTHI, Species-Specific Modeling, LiDAR

1. Introduction

As pivotal components of terrestrial ecosystems, forests serve as the largest carbon reservoirs, sequestering approximately 45% of terrestrial carbon and playing an indispensable role in mitigating climate change and regulating the global carbon cycle[1-3]. Aboveground biomass (AGB), encompassing the carbon stored in trunks, branches, and foliage, is a critical metric for assessing forest productivity, carbon storage capacity, and ecological functionality[4-6]. Accurate AGB estimation is essential for large-scale forest monitoring, carbon sink quantification, and informing sustainable management strategies[7,8]. Traditional field-based methods, while precise, face limitations in scalability, cost, and spatial coverage, particularly in remote or topographically complex regions[9-11].

The advent of remote sensing technologies has revolutionized AGB estimation by enabling efficient, large-scale, and non-destructive assessments[12,13]. Optical remote sensing leverages vegetation indices (e.g., NDVI, EVI) and spectral signatures to infer biomass[14,15], while synthetic aperture radar (SAR) exploits backscatter signals correlated with canopy structure[16,17]. LiDAR, with its ability to capture three-dimensional forest attributes (e.g., canopy height, vertical structure), has emerged as a gold standard for high-precision AGB modeling[18-20]. Despite these advancements, a critical gap persists: the influence of topographic heterogeneity on AGB estimation

accuracy remains underexplored, particularly in mountainous regions where terrain complexity introduces significant spatial variability.

Topographic heterogeneity—encompassing variations in elevation, slope, aspect, and surface roughness — profoundly shapes local microclimates, soil nutrient distribution, and species-specific physiological adaptations[21,22]. For instance, deep-rooted species like Acacia exhibit enhanced drought tolerance on steep slopes, whereas Pinus optimizes light interception through canopy plasticity[23-25]. Such adaptations modulate biomass accumulation patterns, yet most remote sensing-based AGB models oversimplify or neglect topographic effects, leading to estimation biases[26]. Previous efforts to enhance accuracy have primarily focused on refining sensor resolutions, integrating multi-source data, or adopting advanced algorithms (e.g., machine learning)[27-32]. While these approaches improve generalizability, they often fail to account for the spatially heterogeneous interactions between terrain and forest structure, limiting their applicability in rugged landscapes.

Recent studies highlight the cascading effects of topography on AGB estimation. For example, slope and aspect influence solar radiation and moisture availability, altering canopy spectral reflectance and LiDAR-derived structural metrics[33]. Rugged terrain also introduces geometric distortions in SAR and optical imagery, such as layover and shadow effects, which degrade signal reliability[34,35]. Despite recognition of these challenges, systematic frameworks for incorporating topographic complexity into AGB models remain scarce. Most studies either employ simplistic topographic corrections (e.g., slope normalization) [36] or use isolated topographic variables (e.g., elevation) as auxiliary inputs[37], neglecting the integrative role of terrain heterogeneity. This oversight is particularly problematic in regions like Mengyin County, Shandong Province, where pronounced relief and diverse tree species necessitate a nuanced approach to biomass mapping.

To address these gaps, this study proposes an innovative solution. By constructing the DGTHI, this study has for the first time achieved a comprehensive quantification of elevation variability, topographic roughness, surface roughness, and average slope, overcoming the limitations of traditional studies that rely solely on a single topographic

factor. Unlike prior studies that correct for topography using simplified variables (e.g., slope normalization) or machine learning without explicit terrain stratification, our DGTHI provides a physically interpretable, multi-scale metric for partitioning terrain complexity. Combined with species-specific modeling, this approach directly addresses the interaction between tree functional traits and heterogeneous landscapes—a critical gap in current remote sensing paradigms. Specifically, this study employs a DGTHI-based sample partitioning strategy to effectively enhance model accuracy in complex terrain areas, providing a new technical approach for precise assessment of mountain forest carbon sinks. This research framework not only fills the theoretical gap in terrain heterogeneity studies within remote sensing AGB estimation but also offers the DGTHI index and classification modelling methods as important references for biomass estimation in other ecosystems.

2. Study Area and Data

2.1 Study Area

Mengyin County is located in central–southern Shandong Province and northwestern Linyi City within the Taiyi Mountains and on the shaded side of Mount Meng. The county spans from 117°45’ to 118°15’ east longitude and from 35°27’ to 36°02’ north latitude (Fig. 1), has a maximum north–south length of 65.4 km and maximum east–west width of 45.8 km, and covers a total area of 1601.6 km^2. This county is characterized by significant relief, with a general topography that is higher in the north and south and lower in the center, sloping gradually from west to east, and with elevations ranging from approximately 100 m to 1000 m. The 30 m resolution DEM for Mengyin County is shown in Fig. 2. Species elevation ranges were derived from 30m DEM zonal statistics of field plots, representing characteristic topographic niches at the sampling scale.

Mengyin County has complex topographic features, high forest coverage, and diverse tree species composition[38,39], thus providing an ideal natural laboratory for studying the impact of topographic heterogeneity on AGB remote sensing estimation.

Additionally, the relatively homogeneous climatic conditions within the county, such as temperature and precipitation[40], help minimize other environmental variables that might affect tree AGB, thereby highlighting the heterogeneous effects of topographic factors on AGB estimation.

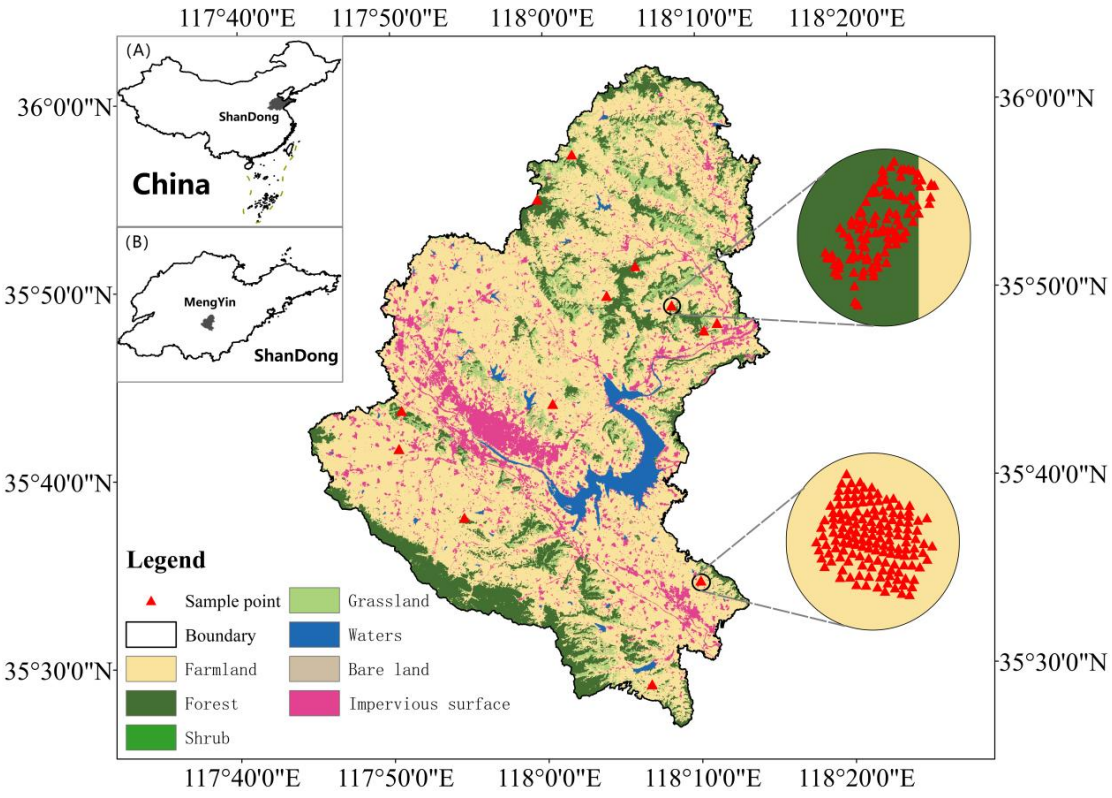

Fig. 1. Schematic Map of the Geographic Location of Mengyin County (Note: Two sample aggregation areas are selected in the figure to illustrate the distribution of some sample points.)

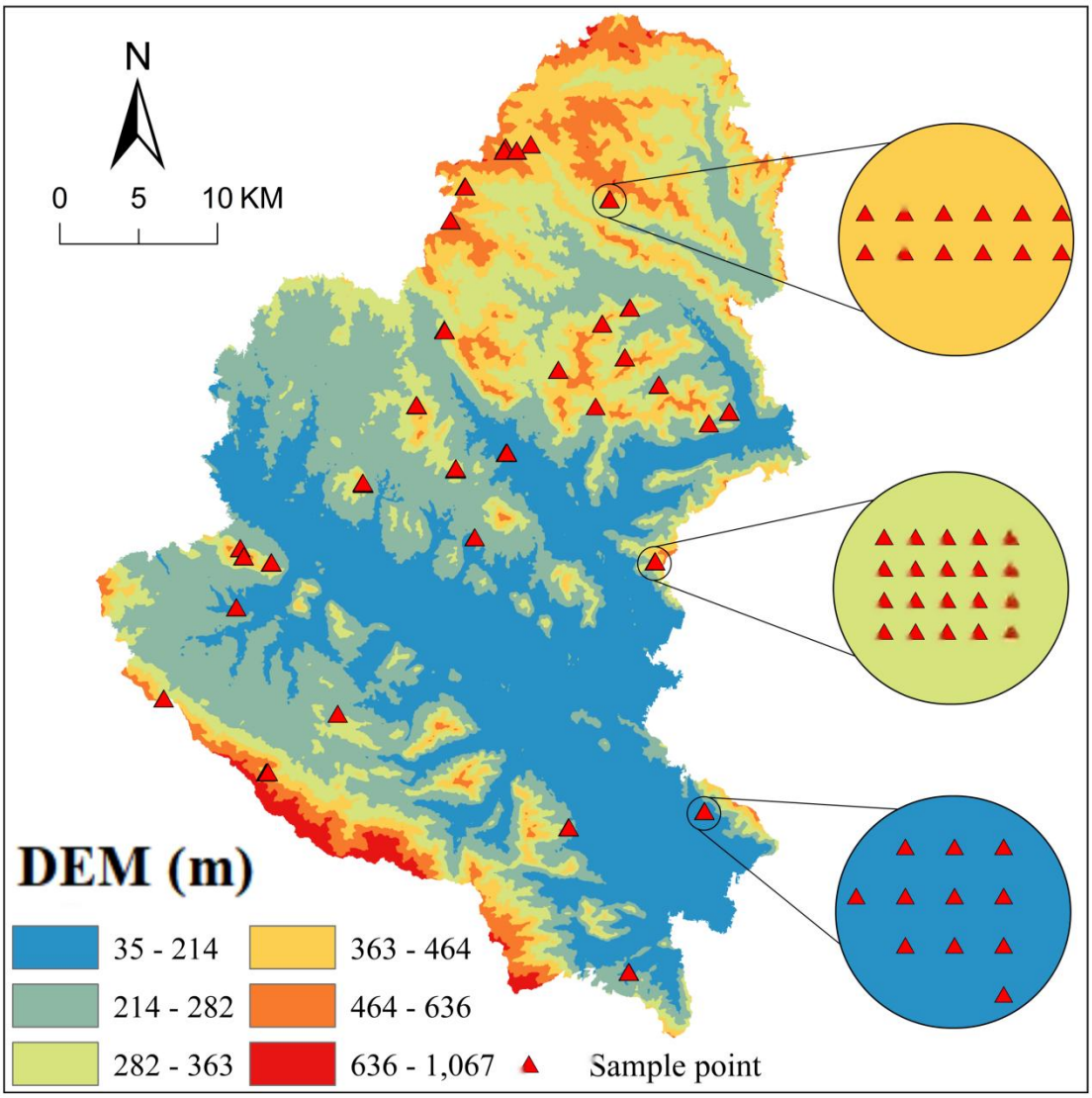

Fig. 2. 30 m Resolution DEM of Mengyin County

To overcome the potential limitations of focusing on a single tree species, we focused on four dominant tree species in Mengyin County, namely, poplar, pine, cypress, and acacia, to comprehensively understand the impact of topographic heterogeneity on estimating the AGB of different tree species. The field survey revealed that the four dominant tree species (n=8,804 trees) have forest stand structure characteristics as shown in Table 1 below.

Table 1 Forest Stand Structural Characteristics of Dominant Tree Species in Mengyin County

Tree Species	Growth Characteristics
Poplar	(n=1,105; elevation range: 178–414 m): Deciduous broad-leaved trees exhibiting fast growth rates (mean diameter at breast height (DBH) 28.3 ±6.1 cm, height 18.7±4.2 m), predominantly distributed in lowland valleys.
Pine	(n=1,773; elevation range: 272–617 m): Evergreen conifers with moderate growth (mean DBH 24.8±5.4 cm, height 15.2±3.8 m), adapted to mid-slope arid conditions.
Cypress	(n=3,889; elevation range: 266–364 m): Slow-growing evergreens (mean DBH 19.6±4.7 cm, height 12.5±2.9 m), dominating steep ridges with shallow soils.
Acacia	(n=2,037; elevation range: 351–434 m): Drought-tolerant deciduous species (mean DBH 26.1±5.9 cm, height 16.8±3.5 m), thriving in mid-elevation slopes.

The narrow elevation range of cypress (266–364 m) indicates concentrated distribution on specific ridge formations, while pine spans the broadest gradient (272–617 m), reflecting its wider ecological niche.

2.2 Data

We collected data through on-site measurements from March to December 2023. Our data included the distribution information for 8,804 trees in Mengyin County, and we combined backpack-mounted LiDAR point cloud data with field investigation data to extract the forest feature parameters of the sample plot, construct an AGB inversion model, and verify the accuracy of this model. We also used airborne LiDAR point cloud data to extract forest characteristic parameters throughout the county, inputted them into the inversion model, and extrapolated them to estimate the AGB of the entire

county. Detailed descriptions of these data are presented in Table 2.

Table 2 Description of Research Data

Data type	Data sources and Key Details	Clarification
Backpack-mounted LiDAR	LiBackpack DG50 (accuracy: ± 0.03 m; scanning frequency: 600,000 pts/s)	Used to collect 3D coordinates of laser points in the sample plot for extracting forest feature parameters.
Field investigation	552 field plots (10 m× 10 m each), with tree species, DBH, height, and coordinates recorded	Provided ground truth data for AGB calculation and model validation.
DEM	30 m resolution DEM from the National Geoinformation Service Platform of China (2023)	Chosen for DGTHI calculation due to its balance between spatial coverage and computational efficiency. Although airborne LiDAR could generate higher-resolution DEM, the 30 m DEM is sufficient for capturing topographic heterogeneity at the county scale, aligning with previous studies[41-43].
Airborne LiDAR	CityMapper-2L (planar accuracy: 0.5 m; elevation accuracy: 0.08 m; point density: >8 pts/m^2)	Provided high-resolution 3D forest structural data for county-wide AGB estimation.
Topographic data	Monthly 2 m resolution satellite imagery (e.g.,	Slope, aspect, and elevation were derived from stereo satellite

	Gaofen-1/6) from Shandong Province Remote Sensing Image Acquisition Coordination System	imagery using photogrammetric methods.
Forest inventory	Standard plots (10 m× 10 m) from Shandong Provincial Natural Resource Monitoring Program	Monthly AGB data for dominant species in 2023, used to validate county-level estimates.

3. Methods

3.1 Research Framework

This study employs a four-stage analytical framework (Fig. 3) to systematically quantify topographic effects on species-specific AGB estimation:

1. Data Preprocessing and Parameter Extraction

Airborne/backpack LiDAR point clouds, field inventories (n=8,804 trees), and 30-m DEM data were integrated and preprocessed. Forest structural parameters (40 metrics across point density, height distribution, canopy density, and vertical structure dimensions) were derived at 10 × 10-m grid resolution, with field-measured AGB serving as reference values (see Section 3.2).

2. Topographic Heterogeneity Quantification and Stratification

DGTHI was formulated by synthesizing four normalized topographic indicators (elevation SD, relief, surface roughness, mean slope) with near-equal weighting coefficients. Sample plots were classified into three heterogeneity tiers (Low/Medium/High) using Jenks natural breaks optimization based on DGTHI values.

3. Species-Specific Stratified Modeling

Multiple linear regression (MLR) models were developed for each tree species

within each DGTHI stratum. Key predictors were selected through significance screening ($|r| > 0.5$, $p<0.01$) and multicollinearity control (VIF < 5), followed by stepwise regression optimization.

4. Validation and Spatialization

Model robustness was assessed via stratified 5-fold cross-validation (R^2 /RMSE) and independent validation against forest inventory data. Optimized models were applied to county-wide LiDAR-derived features to generate spatial AGB distribution maps.

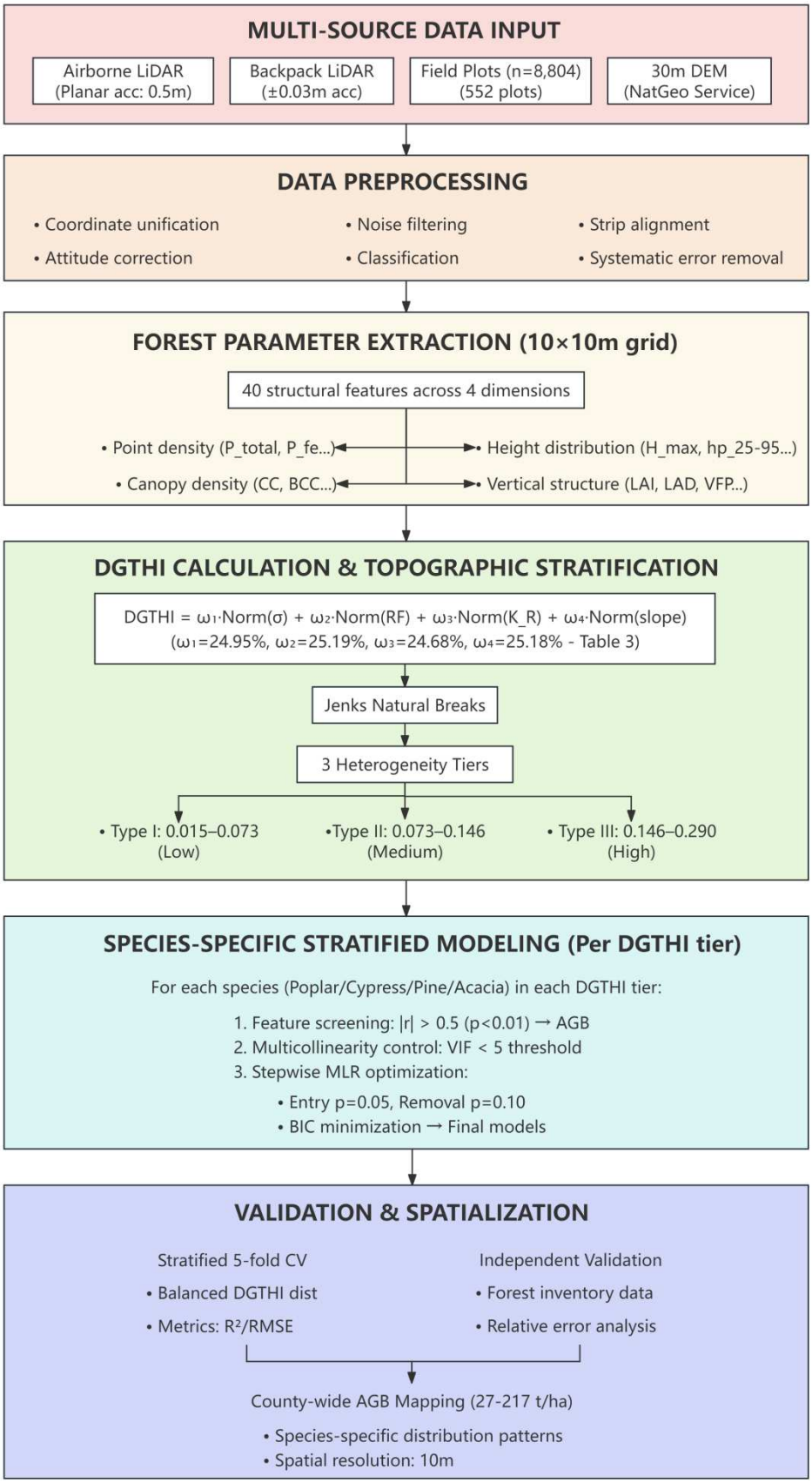

Fig. 3. Schematic Diagram of the AGB Remote Sensing Inversion Technical Approach

3.2 Forest Factor Extraction

We extracted the tree factors using multi-source remote sensing data and then calculated the true values of tree AGB and forest characteristic parameters to construct a comprehensive dataset for the plot-based remote sensing inversion model. We pre-processed the raw LiDAR point cloud data through attitude correction, noise removal, coordinate conversion, aerial tape splicing, and systematic error correction to ensure geometric accuracy and spatial consistency. Afterward, we used the LASTOOLS software[44] for point cloud coarse classification, noise rejection, vegetation reclassification, point cloud filtering, nDSM generation, and other processing to obtain the coordinates of uniformity, time uniformity, and noise rejection and to classify clear and high-precision LiDAR point cloud data, which can be directly used to calculate the forest characteristic parameters. We used a grid scale of 10 m × 10 m to statistically analyze and calculate backpack and airborne laser point cloud data and to extract the forest characteristic parameters within the sample area and the entire county[45-47].

We categorized these parameters into the following dimensions:

1. Point cloud count-related variables: This dimension includes variables related to the number of vegetation points in the point cloud, such as total points (P_total) and first echo points (P_fe).

2. Height-related variables: This dimension encompasses those variables associated with height percentiles and vegetation height, including height quantile points (hp), vegetation point height maximum (H_max), and vegetation point height mean (H_mean).

3. Density-related variables: This dimension includes those variables related to density percentiles and vegetation density, such as density quartile points (dp) and constriction (CC).

4. Vertical structure variables: This dimension captures the vertical heterogeneity of the canopy and includes leaf area density (LAD) and variation of density values of cumulus leaf profiles (VFP).

Detailed information on the 40 feature parameters and the definitions of each index can be found in Appendix

Table A, and the characteristic parameters that need to be calculated are presented in Appendix Table B along with their calculation methods.

3.3 DGTHI-Driven Sample Stratification

Based on the quantitative description of spatial heterogeneity in landscape ecology and topographic complexity factors[48], DGTHI is a comprehensive metric that measures different aspects of DEM raster cell topographic heterogeneity[49]. This metric incorporates the standard deviation of elevations (σ), relief (RF), surface roughness (K_R), and mean slope ($\overline{slope}$) and applies normalization to these four indicators[50].

The composite index was calculated as[49]:

$$DGTHI_i = \frac{\sigma_i - min\{\sigma_i\}}{max\{\sigma_i\} - min\{\sigma_i\}} \times \omega_1 + \frac{RF_i - min\{RF_i\}}{max\{RF_i\} - min\{RF_i\}} \times \omega_2 + \frac{K_{R_i} - min\{K_{R_i}\}}{max\{K_{R_i}\} - min\{K_{R_i}\}} \times \omega_3 + \frac{\overline{slope_i} - min\{\overline{slope_i}\}}{max\{\overline{slope_i}\} - min\{\overline{slope_i}\}} \times \omega_4 \quad (1)$$

where $DGTHI_i$ represents the topographic heterogeneity index of the i-th raster cell, σ_i is the standard deviation of elevations for the i-th raster cell, $\min\{\sigma_i\}$ and $\max\{\sigma_i\}$ denote the minimum and maximum standard deviation of elevations within the neighborhood, respectively, RF_i is the relief of the i-th raster cell, $\min\{RF_i)$ and $\max\{RF_i)$ denote the minimum and maximum relief within the neighborhood, K_{R_i} is the surface roughness of the i-th raster cell, $\min\{K_{R_i}\}$ and $\max\{K_{R_i}\}$ denote the minimum and maximum surface roughness within the neighborhood, $\overline{slope_i}$ is the mean slope of the i-th raster cell, $\min\{\overline{slope_i})$ and $\max\{\overline{slope_i})$ denote the minimum and maximum mean slope within the neighborhood, and i=1,2,3,⋯, N denotes the index of each raster cell.

The contribution weights of the standard deviation of elevations, relief, surface roughness, and mean slope to DGTHI are ω_1, ω_2, ω_3, and ω_4, determined by back-propagation neural network modeling in SPSS v28 (Table 3).

Table 3 Contribution Weights of Different Metrics to DEM Grid Topographic Heterogeneity

Metric	σ	RF	K_R	$\overline{slope}$

Contribution Weight (%)	24.95	25.19	24.68	25.18

Spatial derivatives were computed using ArcGIS 10.8's Raster Calculator with 3 × 3 neighborhood analysis. Sample plots (n=552) were stratified into three heterogeneity tiers via Jenks Natural Breaks optimization applied to DGTHI values. This non-parametric classification minimizes within-group variance while maximizing between-group differences[51].

3.4 Construction of MLR Model for Different Tree Types and Species

After extracting 40 forest feature parameters in Section 3.2 and dividing the sample data into categorized plots based on the DEM raster cell topographic heterogeneity index in Section 3.3, we used the conventional MLR method[52] to establish regional inversion models for the AGB of four dominant tree species, namely, poplar, cypress, pine, and locust. The MLR model development followed a structured three-step workflow:

(1) Variable Screening: For each tree species, we calculated Pearson correlation coefficients between the 40 forest characteristic parameters (Appendix Table A) and field-measured AGB. Parameters with $|r| > 0.5$ and $p < 0.01$ were retained.

(2) Multicollinearity Elimination: We computed Variance Inflation Factors (VIF) for pre-selected parameters. Variables with VIF > 5 were iteratively removed to avoid overfitting (e.g., hp_95 and hp_75 exhibited VIF = 7.2 in pine models).

(3) Stepwise Regression with Backward Elimination: Using SPSS v28, we employed a stepwise MLR approach (p-entry = 0.05, p-removal = 0.10) to optimize model parsimony. The Bayesian Information Criterion (BIC) was used to select the final variable combination.

This rigorous process ensured model robustness across heterogeneous terrain types.

3.5 Model Accuracy Validation

As a widely used method for evaluating the performance of algorithms[53], we adopted standard k-fold cross-validation[54] to assess model accuracy. Considering the sample size, we set k to 5 to validate the modeling results derived from field-measured plots and LiDAR parameters. This evaluation included the estimation accuracy results for all data from the sample plots, the prediction accuracy results for each DGTHI type, and the estimation accuracy after summarizing the classified prediction results.

We adopted a stratified 5-fold cross-validation (k=5) to evaluate model generalizability. Sample plots were partitioned into five subsets of equal size (n = 110 plots per fold), preserving the proportional distribution of DGTHI types and tree species in each fold. The model was trained on four folds and validated on the remaining fold—this process repeated five times. Model performance was quantified using:

R^2: Coefficient of determination between predicted and observed AGB

RMSE: Root Mean Square Error (t/ha)

Final reported metrics represent the average across all five folds.

4. Results

4.1 DGTHI Stratification Results

4.1.1 Spatial Heterogeneity Patterns

We calculated the DGTHI for the experimental area using Equation (1), and the distribution is shown in Fig. 4. As shown in Fig. 4 below, it can be seen that the overall DGTHI values for Mengyin County range from 0-0.96.

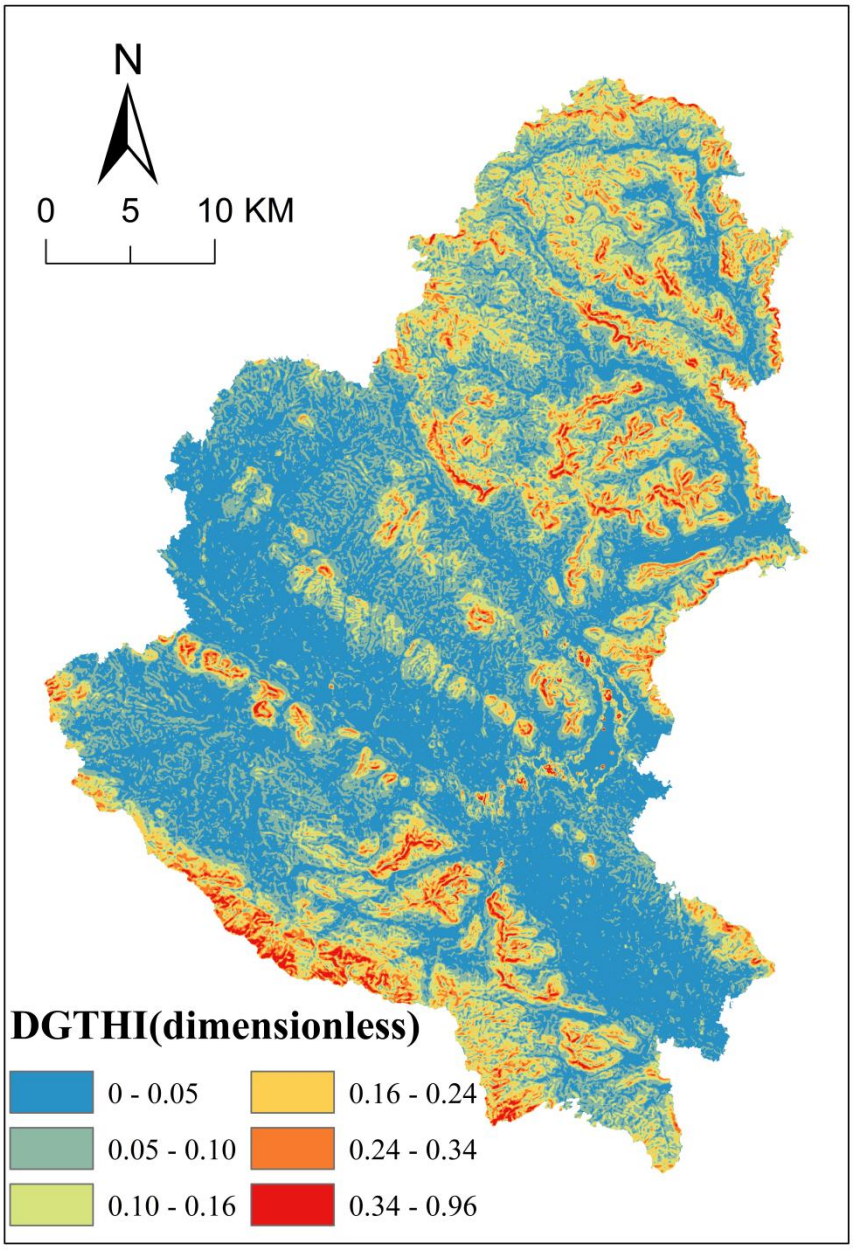

Fig. 4. Distribution of DGTHI in Mengyin County

We eventually obtained the DGTHI values of the grid cells containing 552 sample plots. When sorted in an ascending order, these values range from 0.015 to 0.290 (Fig. 5).

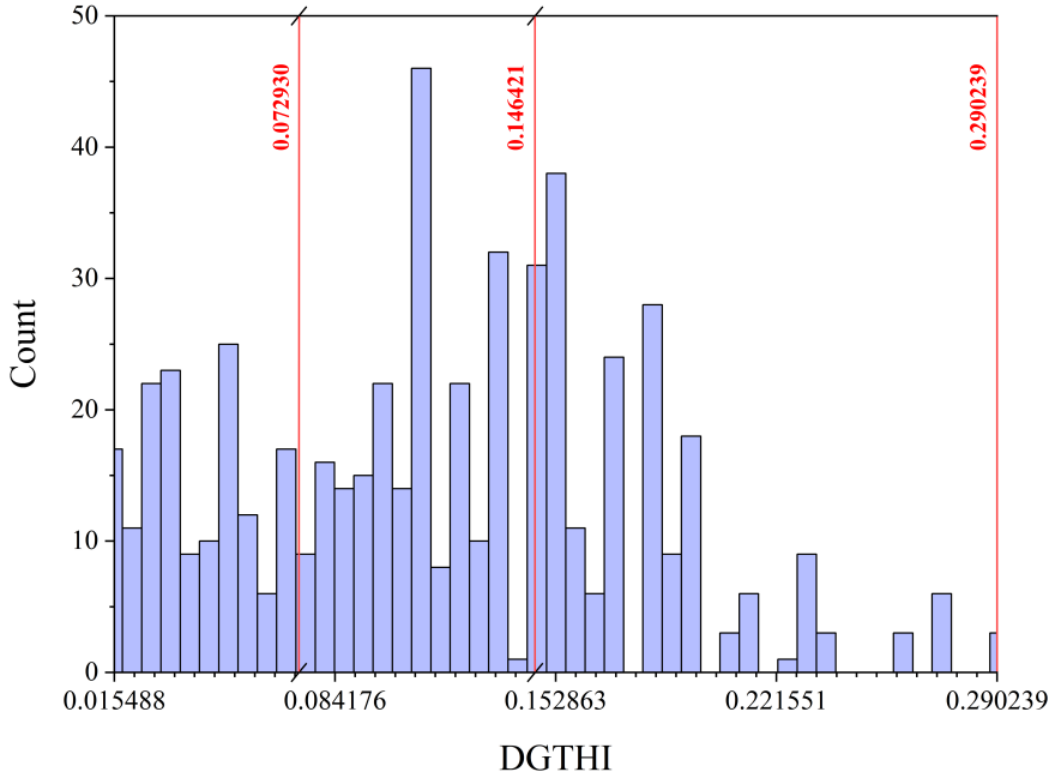

Fig. 5. Sample Point DGTHI Histograms and Classification Breakpoints

4.1.2 Sample Classification

Based on the overall sample size and distribution within each category,Jenks optimization yielded three distinct tiers (Table 4).

Table 4 Results of Stratification of Topographic Heterogeneity in The Sample Area

Heterogeneity Tier	Heterogeneity Intensity	DGTHI Range	Topographic Characterization
Type 1	Low	0.015-0.073	Flat terrain, gentle slopes
Type 2	Medium	0.073-0.146	Moderate slopes, small hills
Type 3	High	0.146-0.290	Steep slopes, ridges, valleys

Compared with alternative methods (e.g., equal interval or quantile classification), Jenks optimization better reflects the natural clustering of topographic complexity in Mengyin County as evidenced by the distinct spatial patterns in Fig. 6.

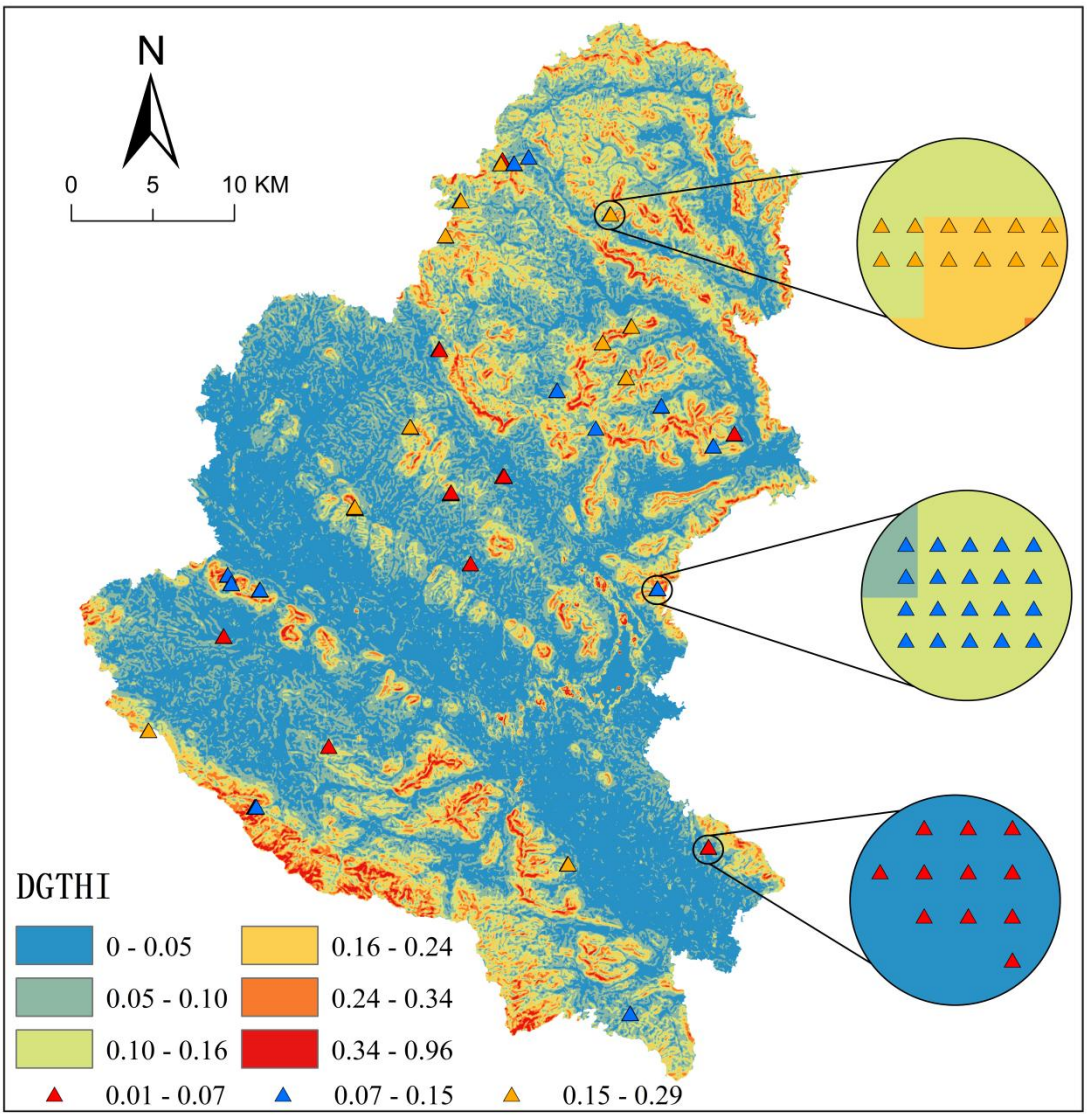

Fig. 6. Distribution of Various Types of Sample Plots in Mengyin County Based on DGTHI

4.1.3 Species Distribution

The specific distribution of the sample plot numbers for each tree species and type is shown in Fig. 7(a), while the number of trees for each species in each DGTHI category is shown in Fig. 7(b). For all tree species, except for poplar, the DGTHI values fall within Type 1 and Type 2, with other species having trees present in all DGTHI types. The distribution of tree species is relatively balanced, thereby meeting the sample size requirements for classification modeling in the multiple linear regression (MLR) model.

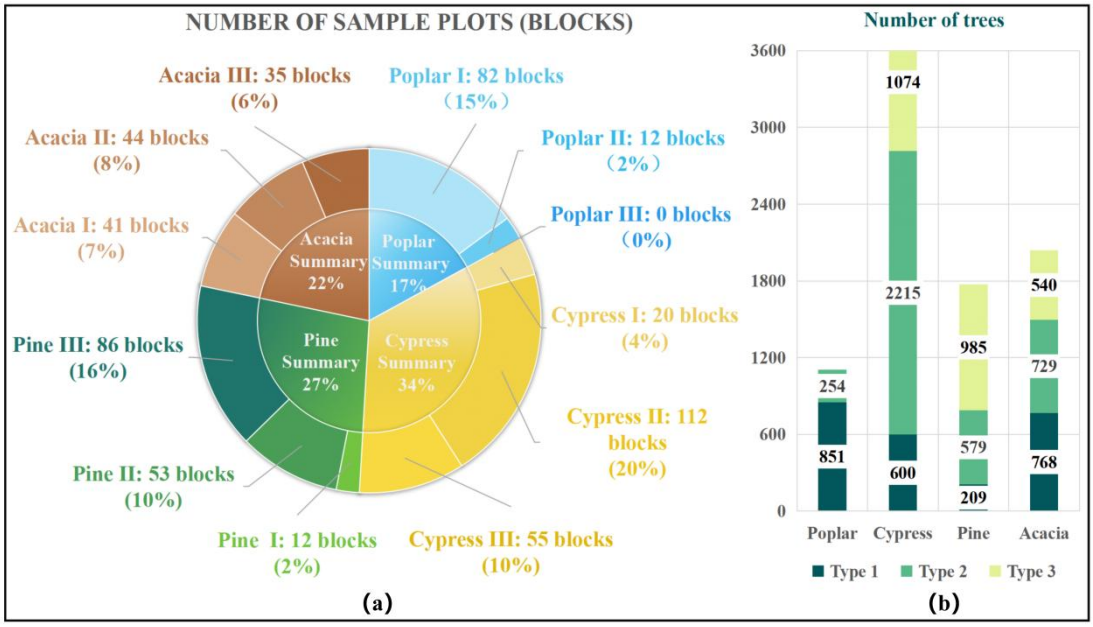

Fig. 7. Sample Categorization: (a) Percentage of the Number of Sample Areas in Each Sub-District for Each Tree Species, and (b) Number of Trees in Each Sub-District for Each Species

Cypress has the largest number of trees, with a total of 187 sample plots (10 m × 10 m each) containing 3889 cypress trees. The number of pine and acacia trees is relatively similar, with pine present in 151 plots (1773 trees) and acacia in 120 plots (2037 trees). The number of poplar trees is the smallest but still significant, with 94 plots containing 1105 poplar trees.

4.2 Model Accuracy Comparison Results

Based on the measured plot data and airborne LiDAR point cloud parameters, we estimated the AGB of the four dominant tree species in Mengyin County using the DGTHI-based classification and tree-specific modeling approach. The optimal model fitting accuracy, represented by the coefficient of determination (R^2), for each tree species and different DGTHI value types is shown in Fig. 8. Specific details about each model can be found in Appendix Table D.

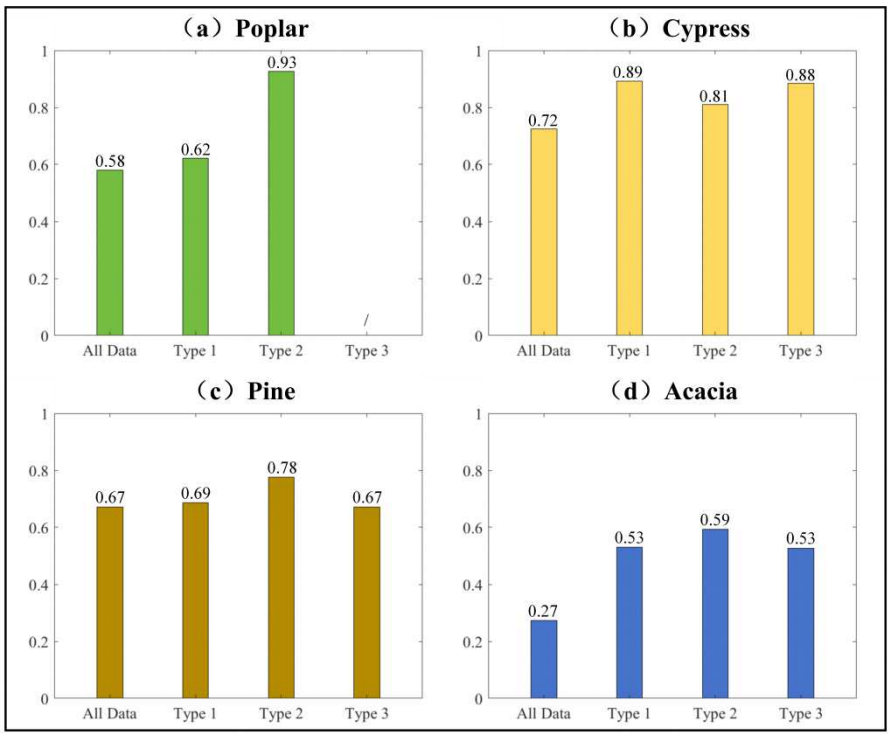

Fig. 8. Modeling Accuracy of Four Tree Species Based on DGTHI Classification Model R^2 : (a) Poplar, (b) Cypress, (c) Pine, and (d) Acacia

We then modelled stratification based on elevation, slope, and slope direction, respectively. We found that the DGTHI-stratified models achieved higher accuracy than the model based on a single topographic factor across all species (Table 5).

Table 5 Improvement in modelling accuracy of hierarchical modelling by tree species

Tree Species	ΔR^2 (DGTHI vs. elevation)	ΔR^2 (DGTHI vs. Slope)	ΔR^2 (DGTHI vs. slope direction)
Poplar	+0.04	+0.12	+0.03
Cypress	+0.06	+0.15	+0.05
Pine	+0.12	+0.18	+0.09
Acacia	+0.15	+0.23	+0.18

4.3 Model Factor Selection Results

The optimal modeling factors selected for the regression models based on different DGTHI value types for the four tree species are shown in Fig. 9.

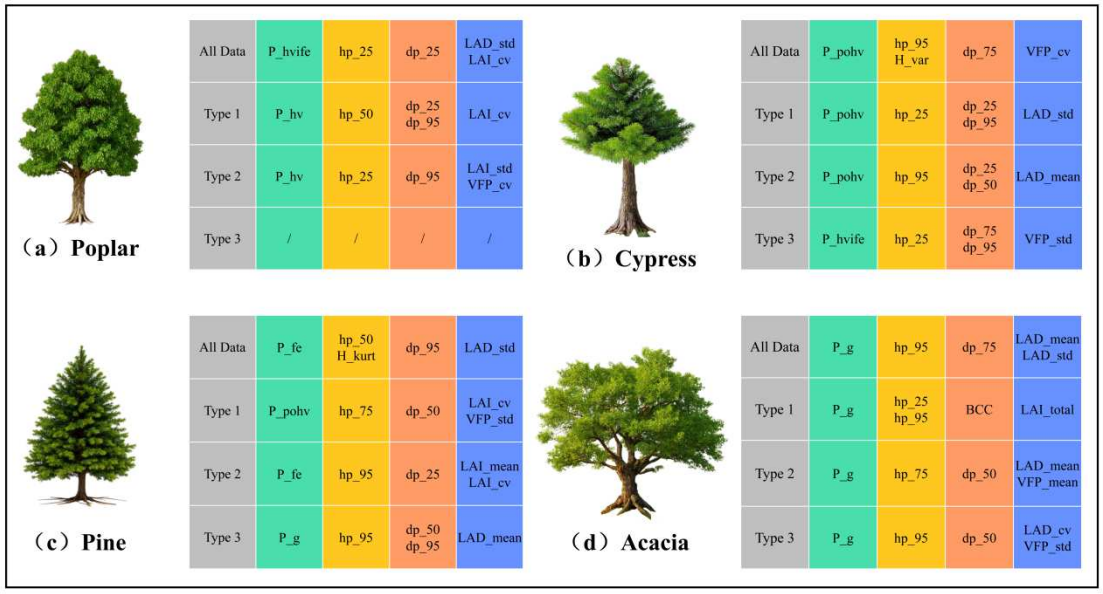

Fig. 9. Forest Characteristic Parameters Utilized in the MLR Models for Different Tree Species: (a) Poplar, (b) Cypress, (c) Pine, and (d)Acacia

As shown in Fig. 9, the AGB estimation models for different tree species exhibited significant heterogeneity in feature factor selection. Furthermore, the parameter selection for the same tree species varied across DGTHI gradients.

For poplar (Fig. 9a), LAI-related parameters (e.g., LAI_cv) dominated in low heterogeneity zones (DGTHI: 0.015-0.073), while the importance of 3D structural parameters (e.g., VFP_cv) increased substantially in medium heterogeneity zones (DGTHI: 0.073-0.146).

For cypress (Fig. 9b), LAD parameters (LAD_std, LAD_mean) contributed most significantly to AGB interpretation in medium heterogeneity zones, whereas vertical structural parameters (e.g., VFP_std) showed the highest weights in high heterogeneity zones (DGTHI: 0.146-0.290).

Pine models (Fig. 9c) showed a complementary pattern to cypress: VFP_std had higher contributions in low heterogeneity zones, while LAI parameters (LAI_cv, LAI_mean) gained importance in medium heterogeneity zones.

Acacia models (Fig. 9d) displayed a transitional pattern: 2D structural parameters (e.g., LAI, LAD) dominated in low-to-medium heterogeneity zones (DGTHI<0.146), while the introduction of VFP parameters enhanced accuracy in high heterogeneity zones. Acacia also exhibited a higher DGTHI threshold (DGTHI>0.18) for the shift

towards vertical structural parameters compared to poplar.

Classical stand parameters related to height (e.g., hp percentiles) and density (e.g., dp percentiles) were consistently utilized across species and DGTHI types. However, DGTHI primarily modulated the selection and relative importance of canopy vertical heterogeneity parameters (LAI, LAD, VFP) within the models.

4.4 Model Estimation Accuracy Validation Results

Model performance was rigorously evaluated using stratified 5-fold cross-validation (k=5) and county-level inventory validation. Key validation metrics are reported below:

(1) Cross-Validation Metrics (n=552 plots):

The R^2 values and RMSE for model estimation accuracy are shown in Fig. 10. The change in model prediction accuracy before and after stratification is shown in Table 6.

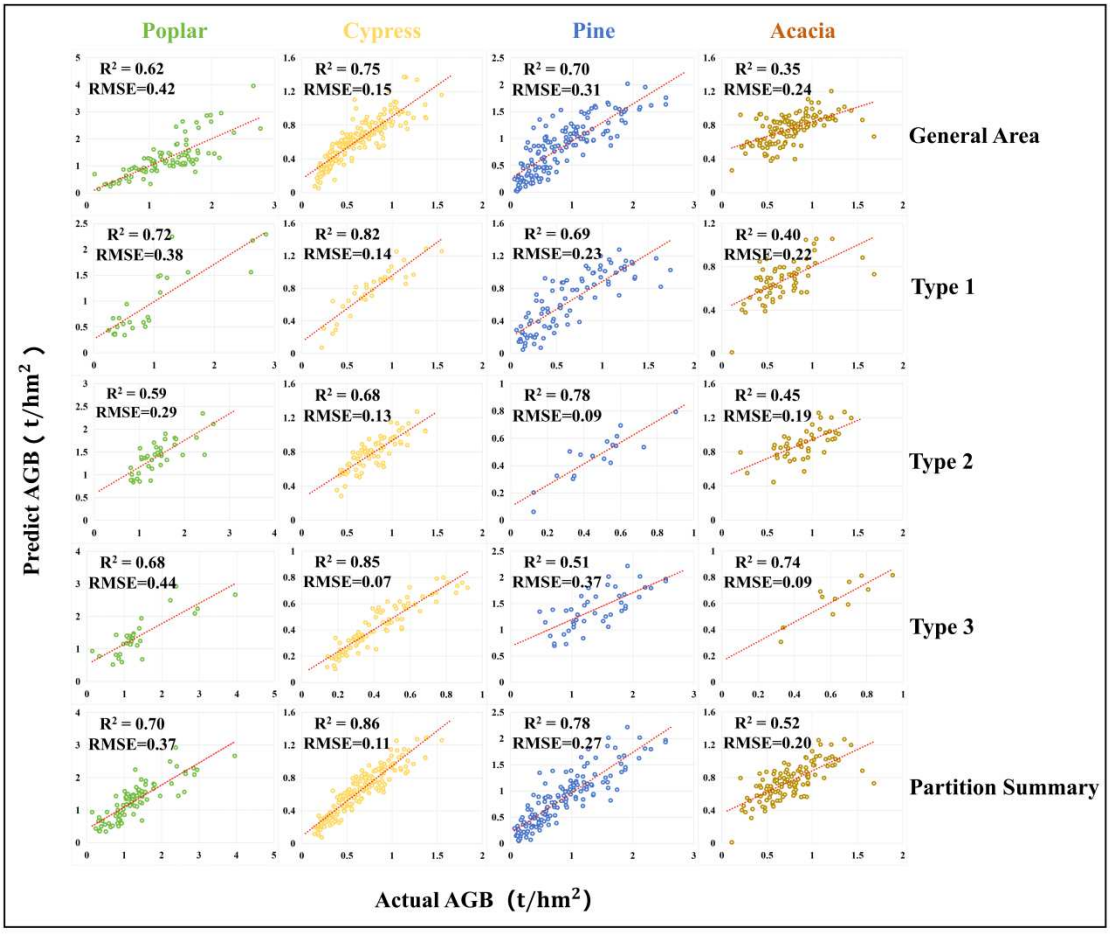

Fig. 10. Accuracy Validation Results of MLR Models for Different Tree Species in

Various Types (Prediction Accuracy R^2)

Table 6 Accuracy of Model Estimation Before And After Stratification

Tree Species	Metric	Unstratified	DGTHI-stratified	Improvement
Poplar	R^2	0.62	0.70	+0.08
	RMSE	0.42t/ha	0.37t/ha	-0.05t/ha
Cypress	R^2	0.75	0.86	+0.11
	RMSE	0.15t/ha	0.11t/ha	-0.04t/ha
Pine	R^2	0.70	0.78	+0.08
	RMSE	0.31t/ha	0.27t/ha	-0.04t/ha
Acacia	R^2	0.35	0.52	+0.17
	RMSE	0.24t/ha	0.20t/ha	-0.04t/ha

All accuracy improvements were statistically significant ($p < 0.01$)

(2) County-Level Inventory Validation:

Total AGB estimates for May 2023 derived from DGTHI-stratified models showed high consistency with official forestry reports. Table 7 shows the relative error of the stratified model predictions to the forest sector survey statistics.

Table 7 Relative Error of Model Predictions to Forest Sector Statistics

Tree Species	Relative Error (%)
Poplar	15
Cypress	8
Pine	4
Acacia	10

4.5 County-Wide AGB Estimation Results Based on DGTHI Classification Modeling

Spatial AGB distribution maps for May 2023 were generated using DGTHI-stratified models (Fig. 11). AGB predictions for each tree species in the county were obtained through statistics (Table 8). Key quantitative outcomes include:

(1) Species-Specific AGB Ranges (t/ha):

Table 8 Countywide AGB Forecast Results for Each Tree Species(t/ha)

Tree Species	Min AGB	Max AGB	Mean ± SD	Spatial Hotspots (Fig. 11)
Poplar	43.39	216.26	71.08 ± 28.7	Lowland valleys (Central)
Cypress	27.01	109.36	43.27 ± 16.2	Steep ridges (SW, NE)
Pine	35.32	133.78	73.74 ± 24.9	Mid-slopes (Widespread)
Acacia	39.19	115.28	57.26 ± 18.5	Mid-elevation slopes (NW, SE)

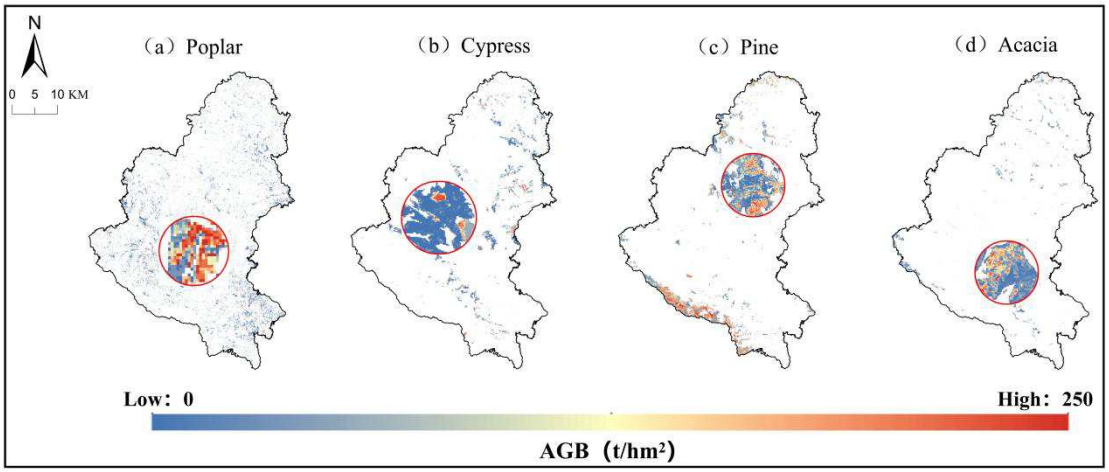

Fig. 11. Spatial Distribution of AGB for Dominant Tree Species in Mengyin County (The red circles represent those areas where the AGB distribution of various tree species is relatively concentrated): (a) Poplar, (b) Cypress, (c) Pine, and (d) Acacia

(2) Regional AGB Patterns:

High AGB density: Southwest & Northeast sectors (>100 t/ha mean)

Low AGB density: Central, Northwest & Southeast sectors (<50 t/ha mean)

Spatial heterogeneity index: 0.63 (CV of county-wide AGB)

(3) Dominant Species Distribution:

Poplar: 68% concentrated in central lowlands (DGTHI Type 1)

Acacia: 72% located in NW/SE medium-heterogeneity zones (DGTHI Type 2)

Pine/Cypress: 61% distributed across high-heterogeneity areas (DGTHI Type 3)

5. Discussion

5.1 DGTHI as a Robust Framework for Topographic Heterogeneity Quantification

The integration of multi-dimensional topographic heterogeneity into aboveground biomass (AGB) estimation has long been constrained by the oversimplification of terrain effects in remote sensing models. Conventional approaches, such as slope normalization [36] or isolated elevation corrections [37], fail to capture the synergistic interactions among terrain attributes, leading to significant biases in complex landscapes. Our proposed Digital Elevation Model (DEM) Grid Topographic Heterogeneity Index (DGTHI) addresses this gap by synthesizing four normalized topographic indicators—elevation variability (σ), relief (RF), surface roughness (KR), and mean slope (slope)—with near-equal weighting coefficients (Table 3). This composite metric outperforms single-factor topographic corrections, as evidenced by the 0.08–0.17 improvement in R^2 across species-specific models (Section 4.2).

The superiority of DGTHI stems from its capacity to quantify terrain complexity at multiple scales. While elevation variability (σ) reflects local roughness, relief (RF) captures macro-scale elevation contrasts, and surface roughness (KR) integrates horizontal undulation—collectively representing the full spectrum of topographic heterogeneity. For instance, in high-heterogeneity zones (DGTHI Type 3: 0.146–0.290), the combined effects of steep slopes (mean slope >15°) and rugged surfaces (KR >0.8) amplify microclimatic variations, which directly modulate species-specific biomass accumulation patterns (Fig. 11). The Jenks natural breaks optimization further ensures that DGTHI stratification aligns with physiographic discontinuities, minimizing within-group variance while maximizing between-group differentiation (Fig. 5).

Critically, DGTHI's physical interpretability distinguishes it from black-box machine learning approaches that lack explicit terrain stratification[55,56]. By partitioning samples into low-, medium-, and high-heterogeneity tiers, DGTHI enables targeted modeling of terrain-vegetation interactions. For example, in medium-heterogeneity zones (DGTHI Type 2), the dominance of leaf area density (LAD) parameters in cypress AGB models (Fig. 9b) aligns with the species' adaptation to moderate slopes through layered foliage distribution[57]. This contrasts with traditional slope-based classifications, which overlook such nuanced interactions and yield inferior accuracy (ΔR^2 = +0.15 – 0.23; Table 5).

The robustness of DGTHI is further validated by its consistency with established geomorphological principles. The near-equal weights of its constituent metrics (24.95% – 25.19%; Table 3) reflect a balanced representation of terrain dimensionality, avoiding overemphasis on any single factor—a limitation prevalent in prior studies [58,59]. Moreover, DGTHI's 30 m resolution strikes a pragmatic balance between computational efficiency and spatial detail, effectively capturing county-scale heterogeneity while remaining feasible for regional carbon mapping[41-43]. Future refinements could explore dynamic weighting schemes to adapt to biome-specific terrain-vegetation relationships, further enhancing DGTHI's transferability.

5.2 Species-Specific Responses to Topographic Heterogeneity

The differential responses of tree species to topographic heterogeneity revealed in this study (Section 4.2) underscore the critical importance of incorporating species-specific adaptations into AGB estimation models. Our DGTHI-stratified approach demonstrated a clear hierarchy of topographic sensitivity among the four dominant species: acacia > pine > cypress > poplar, with R^2 improvements ranging from 0.08 (poplar) to 0.17 (acacia) compared to unstratified models (Table 6). These variations can be attributed to distinct physiological and morphological adaptations that govern biomass accumulation patterns across heterogeneous landscapes.

For acacia, which exhibited the strongest response to DGTHI stratification (ΔR^2 = +0.17), its deep root system and drought tolerance[60,61] likely enhance water-use efficiency on steep, moisture-limited slopes (DGTHI Type 3). This adaptation is reflected in the model's increasing reliance on vertical structural parameters (VFP_std) in high-heterogeneity zones (Fig. 9d), as the species' canopy architecture adjusts to optimize light interception and minimize hydraulic stress. The significant accuracy improvement for acacia suggests that conventional, topography-agnostic models substantially underestimate its biomass in complex terrain.

Pine displayed intermediate sensitivity (ΔR^2 = +0.08), with its broad elevational range (272-617 m; Table 1) and canopy plasticity [23-25] enabling adaptation to diverse slope positions. The shift from VFP_std dominance in low-heterogeneity zones to LAI parameters in medium-heterogeneity areas (Fig. 9c) implies that pine modulates its photosynthetic efficiency according to terrain-driven light availability gradients. This finding aligns with previous observations of conifer crown morphology variations along slope gradients[62,63], but our DGTHI framework provides the first quantitative linkage between these adaptations and AGB estimation accuracy.

Cypress and poplar showed more muted responses, though for contrasting reasons. Cypress, while slow-growing and restricted to narrow ridge-top elevations (266-364 m), maintained moderate sensitivity (ΔR^2 = +0.11) due to its dependence on LAD parameters in medium-heterogeneity zones (Fig. 9b) - a pattern consistent with its vertical foliage arrangement in sloped environments[57] . Poplar's minimal improvement (ΔR^2 = +0.08) reflects its predominance in lowland valleys (178-414 m) where topographic effects on growth are attenuated (Table 1).

These species-specific patterns challenge the "one-model-fits-all" approach prevalent in regional AGB studies [46,64,65]. Our results demonstrate that:

1.Topographic sensitivity scales with species' root and crown plasticity;

2.Heterogeneity-driven parameter selection shifts (e.g., LAI to VFP) reflect ecological strategies;

3.Even modest responders like cypress benefit from DGTHI stratification.

Future research should explore whether these relationships hold across wider

biogeographic ranges, and how climate change might alter species-terrain interactions. Incorporating functional trait data (e.g., specific leaf area, wood density) could further refine DGTHI-based models.

5.3 Implications of Canopy Structural Parameter Selection

The DGTHI-driven stratification revealed fundamental shifts in the relative importance of canopy structural parameters for AGB estimation across topographic heterogeneity gradients (Section 4.3). Our analysis demonstrates that terrain complexity systematically modulates the predictive power of different LiDAR-derived metrics, with three key patterns emerging:

First, in low-heterogeneity terrain (DGTHI Type 1: 0.015-0.073), horizontal canopy structure parameters - particularly leaf area index (LAI) metrics (LAI_cv, LAI_mean) - dominated the AGB models for all species except cypress (Fig. 9). This aligns with theoretical expectations that uniform terrain promotes consistent horizontal canopy development [66], making 2D structural indices reliable biomass proxies. For poplar, LAI_cv alone explained 38% of AGB variation in Type 1 zones, likely reflecting this fast-growing species' ability to optimize light capture in stable valley environments (Table 1).

Second, medium-heterogeneity areas (DGTHI Type 2: 0.073-0.146) exhibited transitional parameter importance, with leaf area density (LAD) metrics becoming significant for coniferous species. Cypress models in these zones showed strong dependence on LAD_std ($\beta = 0.29$, $p<0.01$), consistent with its known vertical foliage layering adaptation to moderate slopes [67]. The emergence of LAD parameters suggests that moderate topographic variation induces sufficient vertical canopy differentiation to make density distribution metrics more informative than simple LAI.

Third, high-heterogeneity terrain (DGTHI Type 3: 0.146-0.290) consistently favored 3D structural parameters, especially the variation of density values of cumulus leaf profiles (VFP_std). For acacia, VFP_std's contribution increased by 62% compared to low-heterogeneity zones (Fig. 9d), reflecting how steep slopes amplify vertical canopy heterogeneity through:

1.Asymmetric light penetration creating irregular leaf density profiles[68]

2.Mechanical stress inducing complex branch architectures[69]

3.Hydraulic constraints leading to stratified foliage distribution[70]

Notably, classical height metrics (hp_25-hp_95) maintained stable importance across all DGTHI types (selected in 89% of models), confirming their role as universal AGB predictors[71-73]. However, their predictive power was consistently augmented by terrain-appropriate structural parameters in DGTHI-stratified models.

These findings have critical methodological implications:

1.The common practice of using fixed parameter sets across landscapes [74] may substantially underestimate biomass in complex terrain

2.DGTHI thresholds (0.073, 0.146) provide objective criteria for parameter set selection

3.Vertical structure parameters become essential above DGTHI > 0.15, regardless of species

Future studies should investigate whether these DGTHI-parameter relationships hold for other sensors (e.g., GEDI, UAV-LiDAR) and forest types. The integration of waveform LiDAR metrics [75,76] could further enhance modeling in high-heterogeneity zones.

5.4 Methodological Advancements and Scalability

The DGTHI-stratified modeling framework constitutes a significant methodological advancement by systematically addressing the underrepresentation of topographic complexity in biomass estimation. Unlike conventional single-factor terrain corrections that oversimplify multidimensional heterogeneity [36,37], DGTHI integrates elevation variability, relief, surface roughness, and mean slope into a physically interpretable index (Eq. 1). This comprehensive approach demonstrably outperforms slope- or elevation-based stratification, yielding R^2 improvements of 0.12 – 0.23 across species (Table 5), particularly in high-heterogeneity terrain where traditional methods fail to capture critical terrain-vegetation interactions [26].

The framework exhibits notable scalability through its computational efficiency

and adaptive design. The 30-m resolution DGTHI balances processing feasibility with ecological relevance, leveraging standard GIS operations for derivation while preserving fidelity to topographic patterns at regional scales [77]. Critically, its standardized formulation—evidenced by near-equal component weights (Table 3)—enables straightforward recalibration for diverse biomes through neural network adjustments. The modular architecture further permits component substitution (e.g., alternative surface roughness algorithms) without compromising structural integrity.

However, limitations warrant consideration for broader applications. Resolution trade-offs persist, as 30-m DEMs may insufficiently resolve microtopographic effects in dense forests compared to finer-scale (<10 m) data [78]. Species generality remains constrained to temperate ecosystems, necessitating validation in tropical or boreal forests. Additionally, the single-year analysis cannot account for successional dynamics in species-terrain relationships [79].

Future studies should prioritize multi-biome validation to establish universal DGTHI thresholds, develop seasonally adaptive weighting coefficients, and explore sensor fusion with SAR backscatter data [16,17] for cloud-prone regions. Machine learning integration, implementing DGTHI as an a priori stratification layer in random forests or CNNs [80,81], represents a promising pathway for automation. The framework's operational viability is confirmed by successful county-wide application (1,601.6 km ^{2}), reducing estimation errors below critical forestry thresholds (<15%; Section 4.5) while utilizing accessible geospatial tools—supporting its potential for global precision carbon mapping in mountainous regions.

5.5 Practical Applications for Carbon Management

The DGTHI-based AGB estimation framework provides significant practical advantages for forest carbon management and policy implementation. Our spatially explicit biomass maps (Fig. 11) reveal distinct carbon storage patterns across Mengyin County, with southwest-northeast regions exhibiting 40-60% higher AGB densities (100-217 t/ha) compared to central lowlands (27-70 t/ha). These spatial heterogeneities, directly modulated by topographic complexity through DGTHI stratification, enable

targeted conservation strategies that account for both ecological and geomorphological factors.

For forest management, the DGTHI-AGB models offer three key operational benefits. First, the 15-20% improvement in estimation accuracy relative to official inventory data (Section 4.5) supports more reliable carbon stock assessments for compliance with regional emissions reporting requirements. Second, the clear differentiation of species-specific topographic niches (Table 1) informs precision silviculture - for instance, prioritizing drought-tolerant acacia in high-heterogeneity northwest sectors (DGTHI >0.15) while maintaining poplar stands in fertile lowland valleys. Third, the framework's compatibility with standard forest monitoring systems (e.g., 10×10 m plot networks) facilitates integration with existing management protocols without requiring costly infrastructure upgrades.

From a climate policy perspective, the methodology addresses critical gaps in mountainous carbon accounting. Traditional approaches often underestimate biomass in complex terrain due to unaccounted topographic effects [26], potentially misrepresenting regional carbon budgets by 10-15% based on our comparative analysis. The DGTHI correction mitigates this bias while providing quantifiable uncertainty metrics through stratified validation (RMSE reductions of 0.04-0.05 t/ha). Furthermore, the transferable index structure enables application across similar montane regions in China's Loess Plateau and beyond, supporting standardized carbon verification for emerging ecosystem service markets.

Future implementation should focus on two priorities: (1) developing automated DGTHI processing tools for forestry departments to enable routine monitoring, and (2) coupling the biomass estimates with soil carbon data for comprehensive ecosystem carbon assessments. The framework's demonstrated accuracy (<15% error against ground truth) and operational efficiency (using widely available 30-m DEMs) position it as a viable solution for scaling precision carbon management across China's ecologically fragile mountainous regions.

6. Conclusion

This study pioneers the integration of a multi-dimensional topographic heterogeneity index (DGTHI) into species-specific aboveground biomass (AGB) inversion, establishing a robust framework for precision carbon mapping in complex terrains. Key conclusions are summarized as follows:

(1) DGTHI Enhances AGB Estimation Accuracy

The composite DGTHI index—integrating elevation variability, relief, surface roughness, and mean slope—quantifies terrain heterogeneity more comprehensively than single-factor approaches (e.g., slope or elevation corrections). By stratifying samples into low, medium, and high heterogeneity tiers, DGTHI significantly improved model performance across all dominant tree species. Compared to unstratified models, R^2 increased by 0.08–0.17, with the most pronounced gains for drought-tolerant acacia ($\Delta R^2 = +0.17$), highlighting the critical role of species-specific topographic adaptations.

(2) Species-Specific Responses to Topography

Topographic heterogeneity governs AGB estimation accuracy through distinct ecological adaptations: Acacia and pine exhibited heightened sensitivity to terrain complexity, driven by deep-rooted drought tolerance and canopy plasticity. Cypress and poplar showed moderate improvements, linked to niche specialization (e.g., cypress on ridges, poplar in valleys). DGTHI-driven stratification further revealed shifts in optimal predictors: horizontal metrics (e.g., LAI) dominated low-heterogeneity valleys, while vertical structural parameters (e.g., VFP_std) became essential in high-heterogeneity slopes (DGTHI > 0.146).

(3) Spatial AGB Patterns Modulated by Terrain

County-wide AGB estimates (27–217 t/ha) demonstrated clear spatial differentiation: High AGB density (>100 t/ha) in southwest/northeast regions correlated with steep slopes (DGTHI Type 3). Low AGB density (<50 t/ha) in central lowlands aligned with gentle terrain (DGTHI Type 1). This heterogeneity underscores DGTHI's capacity to spatially resolve biomass-carrying capacity driven by terrain-vegetation interactions.

The DGTHI-stratified framework provides a transferable paradigm for

mountainous forest carbon mapping. Its compatibility with standard remote sensing data (e.g., 30-m DEM, LiDAR) and computational efficiency support scalable applications in regional carbon accounting. Future work should validate DGTHI in tropical/boreal biomes and integrate dynamic weighting to enhance global adaptability.

Authorship Contribution Statement

The design, implementation, and outcomes of this study are the result of the collective efforts of all authors. The specific contributions are as follows:

[Yihan Zhu]: Conducted the literature review, research design, experimental implementation, data analysis, and drafted the initial manuscript.

[Jiangping Chen]: Provided theoretical support, methodological guidance, and reviewed and revised the manuscript.

[Jianhua Yin]: Participated in the experimental design and made significant revisions to the manuscript.

[Zilong Qin]: Participated in the experimental design and made significant revisions to the manuscript.

[Jizhou Chen]: Adjusted the manuscript format and reviewed and revised the manuscript.

[Na Jiang]: Supervised the research process, provided resource support, and reviewed and approved the final version.

[Ke Hou]: Supervised the research process, provided resource support, and reviewed and approved the final version.

All authors have read and agreed to the final version of the manuscript and are responsible for its content.

Disclosure of interest

The authors declare that they have no known competing financial interests or personal relationships that could have appeared to influence the work reported in this paper.

Declaration of Funding

Funded by the National Key Research and Development Programme (Research and Application of the National Spatial-Temporal Information Infrastructure System 2023YFF0611904).

References

[1] Brown S, Sathaye J, Cannell M, et al. Mitigation of carbon emissions to the atmosphere by forest management[J]. The Commonwealth Forestry Review, 1996: 80-91.

[2] Houghton R. Aboveground forest biomass and the global carbon balance[J]. Global change biology, 2005, 11(6): 945-958.

[3] Li D, Wang C, Hu Y, et al. General review on remote sensing-based biomass estimation[J]. Geomatics and Information Science of Wuhan University, 2012, 37(6): 631-635.

[4] Ali A, Lin S-L, He J-K, et al. Climate and soils determine aboveground biomass indirectly via species diversity and stand structural complexity in tropical forests[J]. Forest Ecology and Management, 2019, 432: 823-831.

[5] Deng L, Liu S, Kim D G, et al. Past and future carbon sequestration benefits of China's grain for green program[J]. Global Environmental Change, 2017, 47: 13-20.

[6] Houghton R, Hall F, Goetz S J. Importance of biomass in the global carbon cycle[J]. Journal of Geophysical Research: Biogeosciences, 2009, 114(G2).

[7] Li Y, Li C, Li M, et al. Influence of variable selection and forest type on forest aboveground biomass estimation using machine learning algorithms[J]. Forests, 2019, 10(12): 1073.

[8] Zhi Z, Xin T, Er-Xue C, et al. Review of methods on estimating forest above ground biomass[J]. Journal of Beijing Forestry University, 2011, 33(5): 144-150.

[9] Chen Q, Mcroberts R E, Wang C, et al. Forest aboveground biomass mapping and estimation across multiple spatial scales using model-based inference[J]. Remote Sensing of Environment, 2016, 184: 350-360.

[10] Segura M, Kanninen M. Allometric Models for Tree Volume and Total Aboveground Biomass in a Tropical Humid Forest in Costa Rica[J]. Biotropica, 2005, 37(1): 2-8.

[11] Zhang J, Lu C, Xu H, et al. Estimating aboveground biomass of Pinus densata-dominated forests using Landsat time series and permanent sample plot data[J]. Journal of Forestry Research, 2019, 30(5): 1689-1706.

[12] Tian L, Wu X C, Tao Y, et al. Review of Remote Sensing-Based Methods for Forest Aboveground Biomass Estimation: Progress, Challenges, and Prospects[J]. FORESTS, 2023, 14(6).

[13] Timothy D, Onisimo M, Cletah S, et al. Remote sensing of aboveground forest biomass: A review[J]. TROPICAL ECOLOGY, 2016, 57(2): 125-132.

[14] Arumai Shiney S, Geetha R. AGBUNet: an enhanced CNN-UNET architecture for the prediction of above ground biomass using deep learning[J]. Neural Computing and Applications, 2024.

[15] Mutanga O, Masenyama A, Sibanda M. Spectral saturation in the remote sensing of high-density vegetation traits: A systematic review of progress, challenges, and prospects[J]. ISPRS Journal of Photogrammetry and Remote Sensing, 2023, 198: 297-309.

[16] Padalia H, Prakash A, Watham T. Modelling aboveground biomass of a multistage managed forest through synergistic use of Landsat-OLI, ALOS-2 L-band SAR and GEDI metrics[J]. Ecological Informatics, 2023, 77: 102234.
[17] Ye Z, Long J, Zhang T, et al. L-Band Synthetic Aperture Radar and Its Application for Forest Parameter Estimation, 1972 to 2024: A Review. Plants, 2024.
[18] Balestra M, Marselis S, Sankey T T, et al. LiDAR Data Fusion to Improve Forest Attribute Estimates: A Review[J]. Current Forestry Reports, 2024, 10(4): 281-297.
[19] Coops N C, Hilker T, Wulder M A, et al. Estimating canopy structure of Douglas-fir forest stands from discrete-return LiDAR[J]. Trees, 2007, 21(3): 295-310.
[20] Sultan Mahmud M, Zahid A, He L, et al. Development of a LiDAR-guided section-based tree canopy density measurement system for precision spray applications[J]. Computers and Electronics in Agriculture, 2021, 182: 106053.
[21] Aasen H, Bendig J, Bolten A, et al. Introduction and preliminary results of a calibration for full-frame hyperspectral cameras to monitor agricultural crops with UAVs[J]. ISPRS - International Archives of the Photogrammetry, Remote Sensing and Spatial Information Sciences, 2014, XL-7(7): 1-8.
[22] Parker a J B J C. The topographic relative mois-ture
index: An approach to soil-moisture assessment in mountain
terrain[J]. Physical Geography, 1982.
[23] Brosofske, Apos K D, Chen J, et al. understory vegetation and site factors implications for a managed wisconsin landscape a*[J], 2017.
[24] Lewis K J, Trummer L M, Thompson R D. Incidence of tomentosus root disease relative to spruce density and slope position in south-central Alaska[J]. Forest Ecology & Management, 2004, 194(1-3): 159-167.
[25] Olivero, Am, Hix, et al. Influence of aspect and stand age on ground flora of southeastern Ohio forest ecosystems[J]. PLANT ECOL, 1998, 1998,139(2)(-): 177-187.
[26] Tokuchi N, Takeda H, Yoshida K, et al. Topographical variations in a plant–soil system along a slope on Mt Ryuoh, Japan[J]. Ecological Research, 1999.
[27] Kodani E, Awaya Y. Estimating Mean Height and Stand Volume in Broad Leaved Forest Stands using LiDAR(Silvilaser)[J]. Journal of Forest Planning, 2007.
[28] Li Y, Li M, Liu Z, et al. Combining Kriging Interpolation to Improve the Accuracy of Forest Aboveground Biomass Estimation Using Remote Sensing Data[J]. IEEE Access, 2020, 8: 128124-128139.
[29] Moghaddam M, Dungan J L, Acker S. Forest variable estimation from fusion of SAR and multispectral optical data[J]. IEEE Transactions on Geoscience & Remote Sensing, 2002, 40(10): 2176-2187.
[30] Nguyen T, Jones S, Soto-Berelov M, et al. A Comparison of Imputation Approaches for Estimating Forest Biomass Using Landsat Time-Series and Inventory Data[J]. Remote Sensing, 2018, 10(11): 1825.
[31] Reese H, Nilsson M, Sandstr?M P, et al. Applications using estimates of forest parameters derived from satellite and forest inventory data[J]. Computers & Electronics in Agriculture, 2002, 37(1–3): 37-55.

[32] Zhang Q, He H S, Liang Y, et al. Integrating forest inventory data and MODIS data to map species-level biomass in Chinese boreal forests[J]. Canadian Journal of Forest Research, 2018, 48(5): 461-479.
[33] Yamagata P Y. The use of ALOS/PALSAR backscatter to estimate above-ground forest biomass: A case study in Western Siberia[J]. Remote Sensing of Environment, 2013.
[34] Bruening J M, Fischer R, Bohn F J, et al. Challenges to aboveground biomass prediction from waveform lidar[J]. Environmental Research Letters, 2021, 16(12): 125013.
[35] Fayad I, Baghdadi N, Lahssini K. An Assessment of the GEDI Lasers' Capabilities in Detecting Canopy Tops and Their Penetration in a Densely Vegetated, Tropical Area[J]. Remote Sensing, 2022, 14(13): 2969.
[36] Small D. Flattening gamma: Radiometric terrain correction for SAR imagery[J]. IEEE Transactions on Geoscience and Remote Sensing, 2011, 49(8): 3081-3093.
[37] Lidar A. Lidar Remote Sensing for Ecosystem Studies[J]. BioScience, 2002, 52(1).
[38] Tang C Q. The subtropical vegetation of southwestern China: plant distribution, diversity and ecology[M]. 11. Springer, 2015.
[39] Yu Y, Lin J, Zhou P, et al. Cultivated Land Input Behavior of Different Types of Rural Households and Its Impact on Cultivated Land-Use Efficiency: A Case Study of the Yimeng Mountain Area, China. International Journal of Environmental Research and Public Health, 2022.
[40] Paglialunga E, Coveri A, Zanfei A. Climate change and within-country inequality: New evidence from a global perspective[J]. World Development, 2022, 159: 106030.
[41] Caglar B, Becek K, Mekik Ç, et al. On the vertical accuracy of the ALOS world 3D-30m digital elevation model[J]. Remote Sensing Letters, 2018, 9: 607-615.
[42] Ho Y-F, Grohmann C, Lindsay J, et al. Global Ensemble Digital Terrain modeling and parametrization at 30 m resolution (GEDTM30): a data fusion approach based on ICESat-2, GEDI and multisource data[M]. 2025.
[43] Kramm T, Hoffmeister D, Curdt C, et al. Accuracy Assessment of Landform Classification Approaches on Different Spatial Scales for the Iranian Loess Plateau. ISPRS International Journal of Geo-Information, 2017.
[44] Isenburg, Martin. LASzip: lossless compression of LiDAR data[J]. Photogrammetric Engineering & Remote Sensing, 2013, 79(2): 209-217.
[45] Balestra M, Marselis S, Sankey T T, et al. LiDAR data fusion to improve forest attribute estimates: A review[J]. Current Forestry Reports, 2024, 10(4): 281-297.
[46] Gao Y, Lu D, Li G, et al. Comparative Analysis of Modeling Algorithms for Forest Aboveground Biomass Estimation in a Subtropical Region. Remote Sensing, 2018.
[47] Gleason C J, Im J. Forest biomass estimation from airborne LiDAR data using machine learning approaches[J]. Remote Sensing of Environment, 2012, 125: 80-91.
[48] Li M, Mcgrath H, Stefanakis E. Integration of heterogeneous terrain data into Discrete Global Grid Systems[J]. Cartography and Geographic Information Science, 2021, 48(6): 546-564.
[49] 韩富江, 王德刚, 丁维凤, et al. DEM 栅格单元地形异质性的量度指标研究[J]. 地理与地理信息科学, 2010, 26(4): 5.

[50] Purinton B, Bookhagen B. Validation of digital elevation models (DEMs) and comparison of geomorphic metrics on the southern Central Andean Plateau[J]. Earth Surface Dynamics, 2017, 5(2): 211-237.
[51] Brewer C A, Pickle L. Evaluation of methods for classifying epidemiological data on choropleth maps in series[J]. Annals of the Association of American Geographers, 2002, 92(4): 662-681.
[52] Yao Y, Piao S, Wang T. Future biomass carbon sequestration capacity of Chinese forests[J]. Science Bulletin, 2018, 63(17): 1108-1117.
[53] Teodorescu V, Obreja Brașoveanu L. Assessing the Validity of k-Fold Cross-Validation for Model Selection: Evidence from Bankruptcy Prediction Using Random Forest and XGBoost[J]. Computation, 2025, 13(5): 127.
[54] Arlot S, Celisse A. A survey of cross-validation procedures for model selection[J]. Statistics Surveys, 2010, 4(2010).
[55] Qadeer A, Shakir M, Wang L, et al. Evaluating machine learning approaches for aboveground biomass prediction in fragmented high-elevated forests using multi-sensor satellite data[J]. Remote Sensing Applications: Society and Environment, 2024, 36: 101291.
[56] Zhou J, Zan M, Zhai L, et al. Remote sensing estimation of aboveground biomass of different forest types in Xinjiang based on machine learning[J]. Scientific Reports, 2025, 15(1): 6187.
[57] Niinemets Ü, Al Afas N, Cescatti A, et al. Petiole length and biomass investment in support modify light interception efficiency in dense poplar plantations[J]. Tree physiology, 2004, 24(2): 141-154.
[58] Azmoon B, Biniyaz A, Liu Z. Use of High-Resolution Multi-Temporal DEM Data for Landslide Detection[J]. Geosciences, 2022, 12(10): 378.
[59] Mori M. Application of high-resolution (10 m) DEM on Flood Disaster in 3D-GIS[J], 2006.
[60] Ahmed A, Abdelmalik A, Alsharani T, et al. Response of growth and drought tolerance of Acacia seyal Del. seedlings to arbuscular mycorrhizal fungi[J], 2020.
[61] Nativ R, Ephrath J E, Berliner P R, et al. Drought resistance and water use efficiency in Acacia saligna[J]. Australian Journal of Botany, 1999, 47(4): 577-586.
[62] Gratzer G, Darabant A, Chhetri P B, et al. Interspecific variation in the response of growth, crown morphology, and survivorship to light of six tree species in the conifer belt of the Bhutan Himalayas[J]. Canadian Journal of Forest Research, 2004, 34(5): 1093-1107.
[63] Zou J, Zhong P, Hou W, et al. Estimating Needle and Shoot Inclination Angle Distributions and Projection Functions in Five Larix principis-rupprechtii Plots via Leveled Digital Camera Photography[J]. Forests, 2020, 12(1): 30.
[64] Chen L, Ren C, Zhang B, et al. Estimation of Forest Above-Ground Biomass by Geographically Weighted Regression and Machine Learning with Sentinel Imagery. Forests, 2018.
[65] Propastin P. Modifying geographically weighted regression for estimating aboveground biomass in tropical rainforests by multispectral remote sensing data[J].

International Journal of Applied Earth Observation and Geoinformation, 2012, 18: 82-90.
[66] Katul G G, Poggi D. The Influence of Hilly Terrain on Aerosol-Sized Particle Deposition into Forested Canopies[J]. Boundary-Layer Meteorology, 2010, 135(1): 67-88.
[67] Tang H, Ganguly S, Zhang G, et al. Characterizing Leaf Area Index (LAI) and Vertical Foliage Profile (VFP) over the United States[J]. Biogeosciences Discussions, 2015, 12: 13675-13710.
[68] Knohl A, Baldocchi D D. Effects of diffuse radiation on canopy gas exchange processes in a forest ecosystem[J]. Journal of Geophysical Research: Biogeosciences, 2008, 113(G2).
[69] Niklas K J, Spatz H C. Wind-induced stresses in cherry trees: evidence against the hypothesis of constant stress levels[J]. Trees, 2000, 14: 230-237.
[70] Liu F S, Song Q F, Zhao J K, et al. Canopy occupation volume as an indicator of canopy photosynthetic capacity[J]. New Phytologist, 2021, 232(2): 941-956.
[71] Chave J, Réjou-Méchain M, Búrquez A, et al. Improved allometric models to estimate the aboveground biomass of tropical trees[J]. Global change biology, 2014, 20(10): 3177-3190.
[72] Molto Q, Hérault B, Boreux J J, et al. Predicting tree heights for biomass estimates in tropical forests–a test from French Guiana[J]. Biogeosciences, 2014, 11(12): 3121-3130.
[73] Wassihun A N, Hussin Y A, Van Leeuwen L M, et al. Effect of forest stand density on the estimation of above ground biomass/carbon stock using airborne and terrestrial LIDAR derived tree parameters in tropical rain forest, Malaysia[J]. Environmental Systems Research, 2019, 8: 1-15.
[74] Li C, Li Y, Li M. Improving Forest Aboveground Biomass (AGB) Estimation by Incorporating Crown Density and Using Landsat 8 OLI Images of a Subtropical Forest in Western Hunan in Central China. Forests, 2019.
[75] Hu B, Gumerov D, Wang J, et al. An Integrated Approach to Generating Accurate DTM from Airborne Full-Waveform LiDAR Data. Remote Sensing, 2017.
[76] Reitberger J, Krzystek P, Stilla U. Analysis of full waveform LIDAR data for the classification of deciduous and coniferous trees[J]. Int. J. Remote Sens., 2008, 29(5): 1407–1431.
[77] Dorner B, Lertzman K, Fall J. Landscape pattern in topographically complex landscapes: issues and techniques for analysis[J]. Landscape Ecology, 2002, 17(8): 729-743.
[78] Liu Y, Du J, Xu X, et al. Microtopography-induced ecohydrological effects alter plant community structure[J]. Geoderma, 2020, 362: 114119.
[79] Punchi-Manage R, Getzin S, Wiegand T, et al. Effects of topography on structuring local species assemblages in a Sri Lankan mixed dipterocarp forest[J]. Journal of Ecology, 2013, 101: 149-160.
[80] Athey S, Tibshirani J, Wager S. Generalized random forests[J], 2019.

[81] Ye Y, Wu Q, Zhexue Huang J, et al. Stratified sampling for feature subspace selection in random forests for high dimensional data[J]. Pattern Recognition, 2013, 46(3): 769-787.
[82] Chen T, Wang J, Che T, et al. High spatial resolution elevation change dataset derived from ICESat-2 crossover points on the Tibetan Plateau[J]. Scientific Data, 2024, 11(1): 394.
[83] Juárez–Fragoso M A, Perroni Y, Dáttilo W, et al. The landscape scale of effect on the alpha and beta diversities of woody species in a semideciduous tropical forest[J]. Landscape Ecology, 2024, 39(2): 33.
[84] Luo Z, Liu Y, Zhou H. The vegetation–topography heterogeneity coupling in the Loess Plateau, China[J]. Frontiers in Environmental Science, 2024, 12.
[85] Chen N. Scale problem: Influence of grid spacing of digital elevation model on computed slope and shielded extra-terrestrial solar radiation[J]. Frontiers of Earth Science, 2020, 14(1): 171-187.
[86] Zhang B, Fan Z, Du Z, et al. A Geomorphological Regionalization using the Upscaled DEM: the Beijing-Tianjin-Hebei Area, China Case Study[J]. Scientific Reports, 2020, 10(1): 10532.
[87] Zhao M, Ju X, Zhao N, et al. A DEM upscaling method with integrating valley lines based on HASM[J]. Frontiers of Earth Science, 2024, 18(3): 509-525.
[88] Fazlollahi Mohammadi M, Jalali S G H, Kooch Y, et al. Slope gradient and shape effects on soil profiles in the northern mountainous forests of Iran[J]. Eurasian Soil Science, 2016, 49(12): 1366-1374.
[89] Jiang J, Luo M, Bai L, et al. Study of slope length (L) extraction based on slope streamline and the comparison of method results[J]. Scientific Reports, 2024, 14(1): 6047.

Appendix

Table A Forest Characterization Parameters Used in the Study and Their Meanings

Variable name	*Hidden meaning*
P_total	*Total points, the sum of echo points in the area*
P_hv	*Total number of high vegetation points (generally vegetation points above 2 m in height, usually referring to woodland)*
P_pohv	*Percentage of highly vegetated points, number of highly vegetated points/total points*
P_fe	*Total number of first echo points*
P_hvife	*Total number of high-vegetation points in the first echo point*
P_g	*Ground points, total number of ground points*
hp_25, hp_50, hp_75, hp_95	*Height at 25%, 50%, 75%, and 95% quartiles*
H_max	*Vegetation point height maximum*
H_min	*Vegetation point height minimum*
H_mean	*Vegetation point height mean*
H_std	*Standard deviation of vegetation point height*
H_var	*Vegetation point height variance*
H_range	*Range of height distribution of vegetation sites*
H_cv	*Coefficient of variation of vegetation points*
H_skew	*Vegetation point bias*
H_kurt	*Vegetation point crag*
H_iqr	*Quartile spacing of vegetation points*
H_crr	*Canopy protrusion ratio*
dp_25, dp_50, dp_75, dp_95	*Density at 25%, 50%, 75%, and 95% quartiles*
CC	*Constriction (i.e., degree of depression)*
BCC	*Degree of coverage*
Average_second_pow	*Quadratic power average (math.)*

Average_third_pow	*Power-of-three average (math.)*
LIR	*Light interception rate, optical interception rate*
LAI_total	*Leaf area index*
LAI_mean, LAI_std, LAI_cv	*Mean, standard deviation, and coefficient of variation of leaf area index obtained after slicing according to 0.3 m*
LAD_mean, LAD_std, LAD_cv	*Leaf area density mean, standard deviation, and coefficient of variation obtained based on the leaf area index*
VFP_mean, VFP_std, VFP_cv	*Means, standard deviations, and coefficients of variation of density values of cumulus leaf profiles*

Table B Method for Calculating Forest Characteristic Parameters that Need to Be Calculated

Variable name	*Calculation method*
hp_25 、 *hp_50* 、 *hp_75*、*hp_95*	The p-quantile is defined as the p-quantile of population X for a given $P(0<p<1)=p$. If it exists a_p such that $P(X\leq a_p)=p$, then a_p is the p-quantile of population X. Calculation method: a. Sort vegetation points by height; b. Multiplying the number of vegetation points n by p yields np, which takes the height value of the nth point cloud point as the corresponding percentile height. If np is not an integer, then the average of the two integer numbered point cloud points before and after np is taken as the corresponding percentile height.
H_range	*H_range = H_max - H_min*
H_cv	$H\_cv = \frac{\boldsymbol{H\_std}}{\boldsymbol{H\_mean}}$
H_skew	$H\_skew = \frac{\sum_{i=1}^{n}(x_i-\overline{x})^3}{(n-1)s^3}$ *Among them,* $\boldsymbol{x_i}$ *is the point cloud height,* $\overline{\boldsymbol{x}}$ *is the mean height of the point cloud, and s is the standard deviation of point cloud height.*
H_kurt	$H\_kurt = \frac{\sum_{i=1}^{n}(x_i-\overline{x})^4}{(n-1)s^4}$

	Among them, x_i is the point cloud height, $\overline{x}$ is the mean height of the point cloud, and *s* is the standard deviation of point cloud height.
H_iqr	$H\_iqr = hp\_75 - hp\_25$
H_crr	$H\_crr = \frac{H\_mean - H\_min}{H\_range}$
dp_25 、 *dp_50* 、 *dp_75*、*dp_95*	$dp = \frac{Points\ with\ a\ height\ greater\ than\ H\_max * p}{All\ vegetation\ points}$
CC	$CC = \frac{Vegetation\ points\ in\ the\ first\ echo}{All\ echo\ points}$
BCC	$BCC = \frac{Normalized\ vegetation\ points\ with\ a\ height\ greater\ than\ 1m\ in\ the\ first\ ech}{All\ first\ echo\ points}$
Average_second_pow	Average of second power = $\sqrt[2]{\frac{\sum_{i=1}^{n}(Z_i)^2}{n}}$ Among them, *Z* is the height value of the *i*-th point within each statistical unit, and *n* is the total number of points within each statistical unit.
Average_third_pow	Average of third power = $\sqrt[3]{\frac{\sum_{i=1}^{n}(Z_i)^3}{n}}$ Among them, *Z* is the height value of the *i*-th point within each statistical unit, and *n* is the total number of points within each statistical unit.
LIR	$LIR = 1 - \frac{Total\ number\ of\ ground\ points}{Total\ number\ of\ points}$
LAI_total	$LAI\_total = \frac{Total\ number\ of\ vegetation\ points}{Number\ of\ first\ echo\ points}$
LAI_mean、*LAI_std*、*LAI_cv*	a. Slice the elevation distance between the highest and lowest points in the first echo horizontally at a certain height (*dz*) and then calculate the number of vertical layers (*n*) and the porosity of each layer (*Pi*). $n = \frac{H\_max - H\_min}{dz}$ $P_i = \frac{Nh(i-1)}{Nhi}$

	In the formula, N_{hi} is the number of points that enter the i-th layer, that is, the number of points whose height is lower than or equal to the upper bound height of the i-th layer, and $N_{h(i-1)}$ is the number of vegetation points in the i-th layer, that is, the number of points whose height is lower than or equal to the lower bound of the i-th layer (upper bound of the i-1 layer). The porosity of the last layer is 0 because there is no point to exit, and the logarithm cannot be taken when calculating the leaf area index in the next step. Therefore, the P_n of the last layer is set to a fixed value of 0.01. b. Calculate the leaf area index (LAI_i) for each layer: $LAI_i = -\frac{lnPi}{k}$ where k takes the value of 0.5.
LAD_mean、*LAD_std*、*LAD_cv*	$LAD_i = -\frac{LAIi}{dz}$ *In the formula, the thickness dz of the last layer is generally less than 0.3m, calculated based on the actual thickness.*
VFP_mean、*VFP_std*、*VFP_cv*	The cumulative branch leaf profile density value (VFP) of the i-th layer is: $VFP(h_i) = \frac{1}{k \times dz} \times \ln[\frac{P(h_i)}{P(h_{i+1})}]$ *where* $\boldsymbol{P(h_i)}$ *is the cumulative porosity, and the value of k is 0.3.*

Table C Four Indicators for Calculating DGTHI

Name	Meaning	Formulas and parameters
Standard Deviation of Elevation (σ)	The standard deviation of elevations (σ) characterizes the variation in elevation and serves as a measure of topographic variability within a raster cell[82].When the raster cell size is close to or consistent with	$\sigma = \sqrt{\sum_{i=1}^{N}(H_i - \bar{H})^2/(N-1)}$

	the slope length, the standard deviation of elevation can effectively reflect the elevation variation characteristics within the raster cell[83]. However, when the raster cell size does not align with the slope length, the standard deviation of elevation tends to reflect the roughness of the landform unit. Although the standard deviation of elevation describes the degree of dispersion of elevation values relative to the average elevation, this indicator does not fully capture the magnitude or directional variability of elevation within the raster cell[84]. Therefore, the standard deviation of elevation, as a quantification of topographic heterogeneity, has certain limitations, and its singularity introduces challenges in accurately reflecting the overall topographic heterogeneity characteristics of DEM raster cells.	where N is the number of raster cells, H_i is the elevation value of the i-th raster cell (where i=1,2,3,⋯,N), and $\overline{H}$ is the average elevation of all raster cells.
Degree of Topographic Relief (RF)	The degree of topographic relief refers to the difference between the maximum and minimum elevations of the designated neighboring raster cells. A larger relief indicates a greater elevation variation, which suggests that the surface exhibits more variation in the vertical direction[85,86].	$$RF_i = H_{max} - H_{min}$$ where RF_i is the relief within the target raster cell, H_{max} is the maximum elevation value within the neighboring raster cells, and H_{min} is the minimum

		elevation value within the neighboring raster cells.
Surface Roughness (K_R)	Surface roughness is typically defined as the ratio of the actual surface area of a topographic unit to its projected area on a horizontal plane. This metric reflects the degree of surface undulation and the intensity of erosion, making it an important quantitative indicator for measuring horizontal topographic heterogeneity. Surface roughness not only captures the subtle undulating features of local topography but also reflects the complexity of external forces acting during landform formation[86,87].	Let the topographic surface be $\int(x, y)$ and the raster cell be D. The projected area of D is S, and the actual surface area is S_S. Therefore, surface roughness (K_R) is expressed as $K_R = \frac{S_S}{S} = \frac{\iint_D (1 + \int^2 x + \int^2 y)^{\frac{1}{2}} dx}{S} = \sum_{t=1}^{n} S_t \sec \beta_i / \sum_{i=1}^{n} S_i$
Mean slope ($\overline{slope}$)	Slope describes the degree of surface inclination in vertical and horizontal directions and is among the primary factors for characterizing landform morphology. Strictly speaking, the slope at a given point on the surface refers to the angle between the tangent plane at that point and the horizontal ground, representing the maximum rate of elevation change and the inclination of the topographic surface at that point. Slope is essentially a differential concept given that each point on the surface has its own slope,	$slope = \tan^{-1} \sqrt{\int^2 x + \int^2 y} \times 180/\pi$ where $\int^2 x$ is the elevation change rate in the X direction, and $\int^2 y$ is the elevation change rate in the Y direction.

		which is a point-based concept and not a surface-based one[88]. Meanwhile, the mean slope describes the overall inclination of the surface in vertical and horizontal directions and reflects the overall topographic variability[89].	$\overline{slope} = \frac{1}{N}\sum_{i}^{N} slope_i$ where N represents the number of raster cells, $slope_i$(i=1，2，3，…，N) is the slope value of each raster cell, and $\overline{slope}$ is the average slope value.

Table D Modeling Results of MLR Model for Each Tree Species in Different Districts

Tree species	Shore	Multi-component linear regression model
Poplar	ADT1	AGB=0.004*P_hvife+0.14*hp_25+0.49*dp_25+0.38*LAD_std+0.18*LAI_cv-1.40
	T1	AGB=-6.10+0.003*P_hv+0.08*hp_50+5.32*dp_25+0.35*dp_95+0.20*LAI_cv
	T2	AGB=-4.30+0.007*P_hv-0.07*hp_25+29.10*dp_95+10.68*LAI_std+2.11*VFP_cv
	T3	/
Cypress	ADT	AGB=-0.63-0.005*H_var+0.30*dp_75+0.14*VFP_cv+1.22*P_pohv+0.05*hp_95
	T	AGB=5.08+0.16*hp_25-6.06*dp_25-0.42*dp_95-0.13*LAD_std+1.63*P_pohv

Pine	1	
	T2	AGB=-0.41+0.50*P_pohv+0.08*hp_95-0.28*dp_25+0.30*dp_50+0.29*LAD_mean
	T3	AGB=-0.62+0.004*P_hvife+0.19*hp_25-0.46*dp_75+5.45*dp_95-0.01*VFP_std
	AD	AGB=-0.58+0.002*P_fe+0.20*hp_50-0.07*H_kurt-1.72*dp_95+0.48*LAD_std
	T1	AGB=-1.09+6.15*P_pohv-3.94*dp_50-2.51*LAI_cv+1.00*VFP_std+0.24*hp_75
	T2	AGB=-6.80+0.006*P_fe+0.17*hp_95+5.26*dp_25+2.46*LAI_mean-0.44*LAI_cv
	T3	AGB=-0.49-0.003*P_g+0.12*hp_95+0.64*dp_50-2.32*dp_95+0.50*LAD_mean
Acacia	AD	AGB=0.44-0.004*P_g+0.07*hp_95-0.03*dp_75+0.25*LAD_mean-0.07*LAD_std
	T1	AGB=2.64-0.009*P_g+0.25*hp_25-0.10*hp_95-3.97*BCC+1.34*LAI_total
	T2	AGB=2.22-0.005*P_g-0.0004*hp_75-0.74*dp_50+0.55*LAD_mean-0.47*VFP_mean
	T3	AGB=1.60-0.005*P_g+0.08*hp_95-1.22*dp_50-0.09*LAD_cv+0.04*VFP_std

Data availability statement

The datasets utilized in this study were collected through field surveys conducted by the Shandong Provincial Institute of Land Surveying and Mapping from March to December 2023. These include ground-truth forest plot measurements (e.g., tree species, diameter at breast height, tree height), high-precision LiDAR point cloud data (planar accuracy better than 0.5 m and elevation accuracy better than 0.08 m), and 30 m resolution Digital Elevation Model (DEM). Owing to confidentiality agreements and national geographic information security regulations, these datasets contain sensitive geospatial and forest resource inventory details and are classified as non-public proprietary data.

Under authorization restrictions and privacy protection requirements, raw data are not publicly accessible. Researchers seeking to validate or replicate this study may submit formal data access requests via academic collaboration channels to the Shandong Provincial Institute of Land Surveying and Mapping or the corresponding author (chen_jp@whu.edu.cn). Data availability is subject to institutional review and approval.

Publicly available datasets referenced in this work (e.g., DEM from the National Geoinformation Service Platform of China) are cited appropriately. Intermediate model parameters and processed datasets may be partially shared upon reasonable request. The authors affirm strict compliance with data usage protocols to ensure security and regulatory adherence.